Supporting Information

for

Use of ligand steric properties to control the thermodynamics and kinetics of oxidative addition and reductive elimination with pincer-ligated Rh complexes

Shunyan Gu†, Robert J. Nielsen‡*, Kathleen H. Taylor†, George C. Fortman†, Junqi Chen†, Diane A. Dickie†, William A. Goddard III‡*, T. Brent Gunnoe†*

†Department of Chemistry, University of Virginia, Charlottesville, VA 22904

‡Materials and Process Simulation Center, Department of Chemistry, California Institute of Technology, Pasadena, CA 91125

nielsen@caltech.edu, wag@wag.caltech.edu, tbg7h@virginia.edu

Table of Content

1. NMR Spectra of Complexes

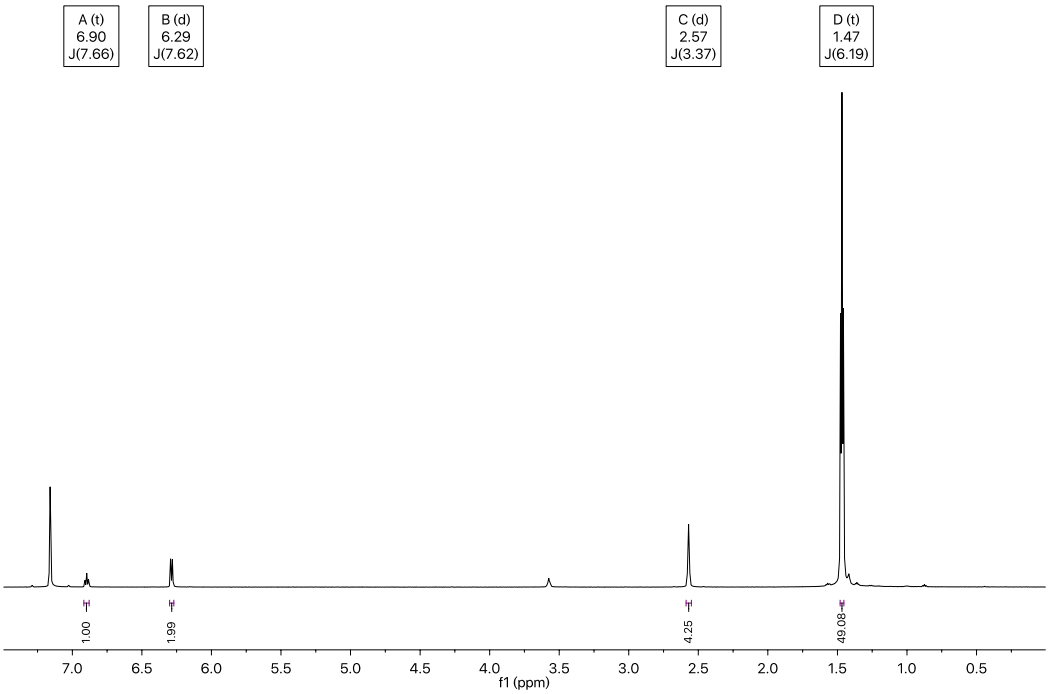

Figure S1. $_{1}$H NMR spectrum of ($_{tBu}$PNP)RhCl (**1a**) (benzene-*d*$_{6}$, 600 MHz).

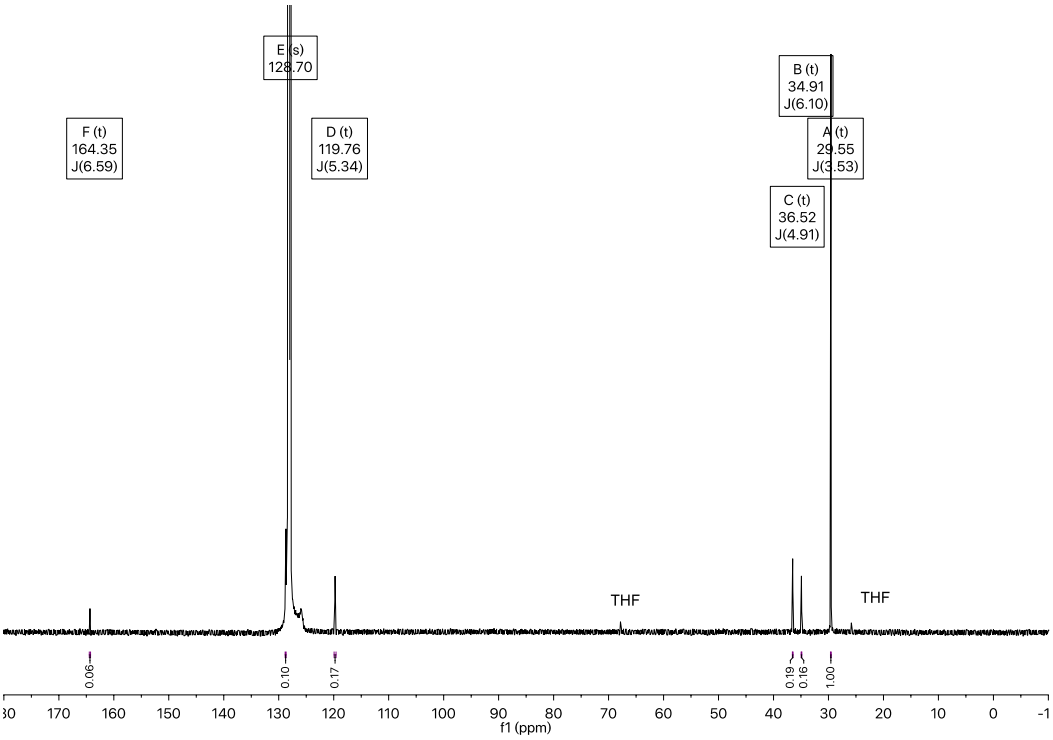

Figure S2. $_{13}$C{$_{1}$H} NMR spectrum of ($_{tBu}$PNP)RhCl (**1a**) (benzene-*d*$_{6}$, 243 MHz).

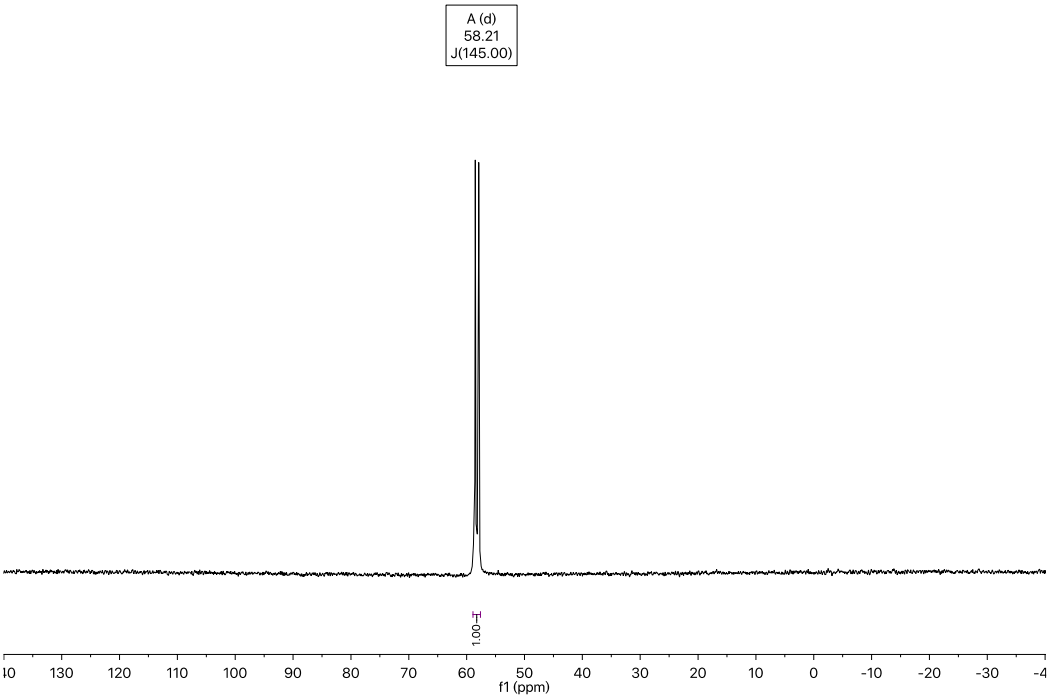

Figure S3. $^{31}P\{^{1}H\}$ NMR spectrum of (^{tBu}PNP)RhCl (**1a**) (benzene-d_6, 151 MHz).

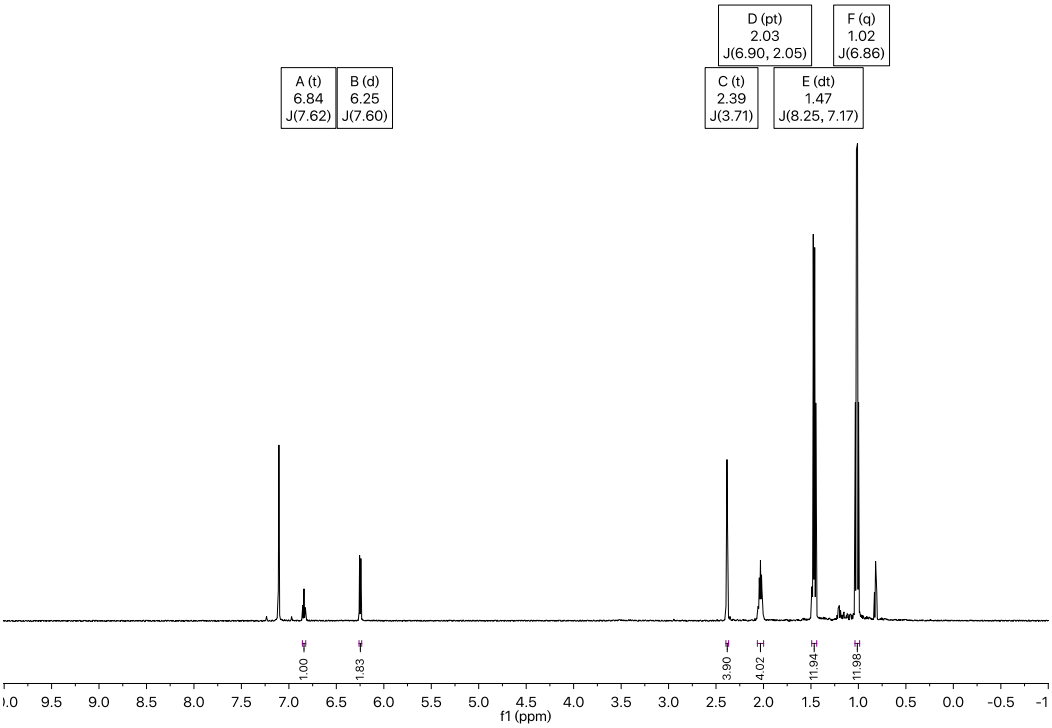

Figure S4. ^{1}H NMR spectrum of (^{iPr}PNP)RhCl (**2a**) (benzene-d_6, 600 MHz).

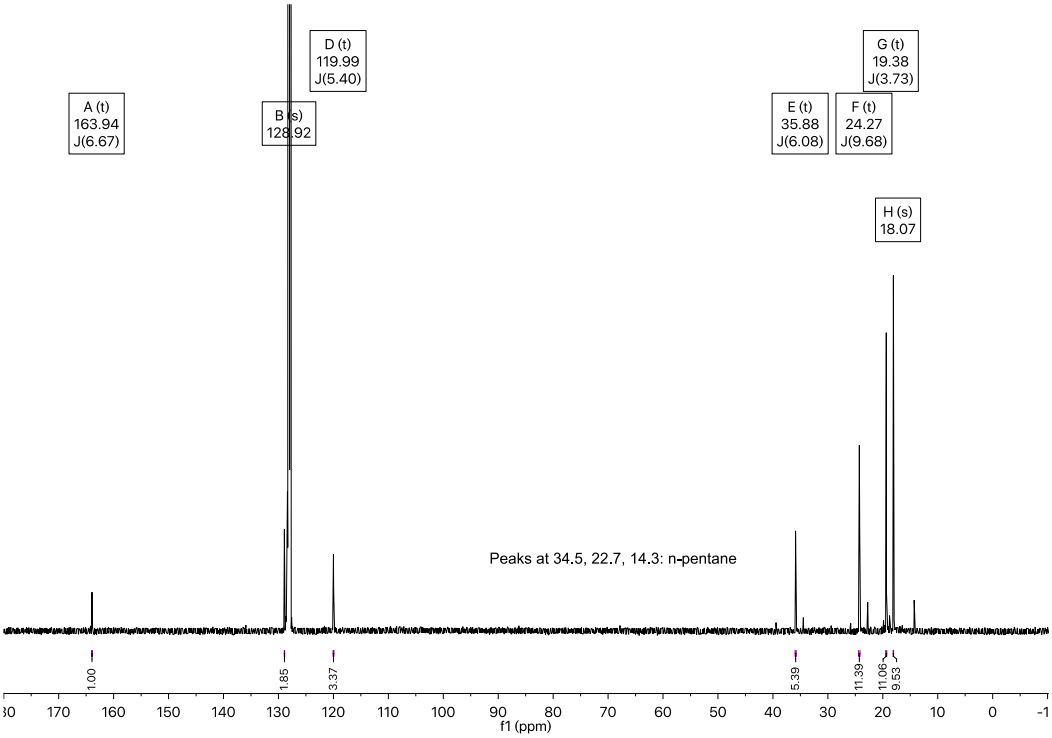

Figure S5. $^{13}C\{^{1}H\}$ NMR spectrum of (^{i}PrPNP)RhCl (**2a**) (benzene-d_6, 243 MHz).

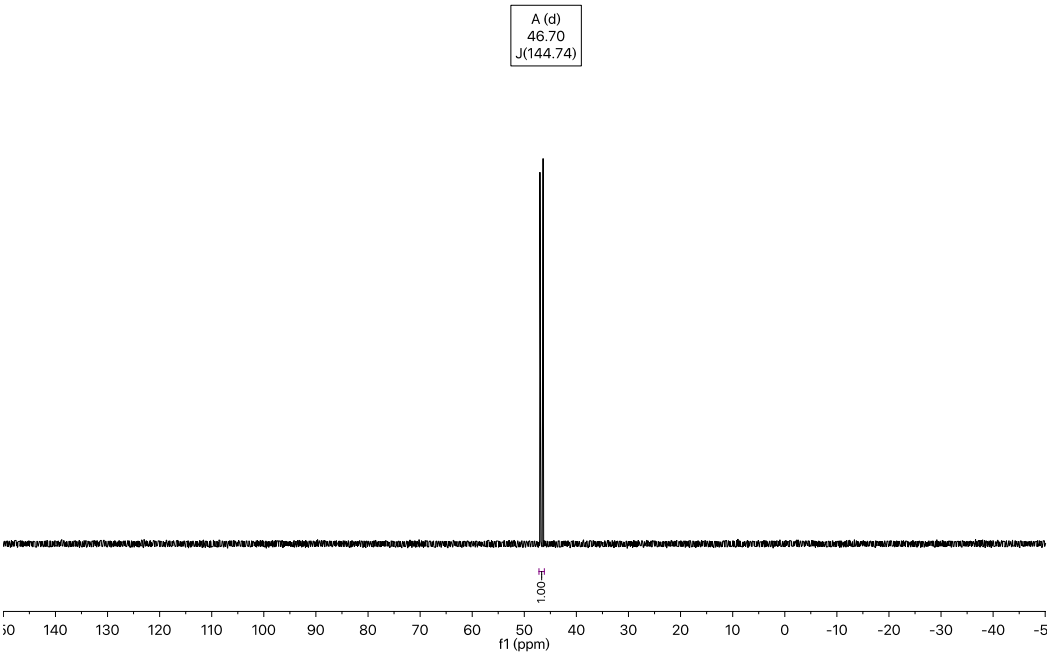

Figure S6. $^{31}P\{^{1}H\}$ NMR spectrum of (^{i}PrPNP)RhCl (**2a**) (benzene-d_6, 151 MHz).

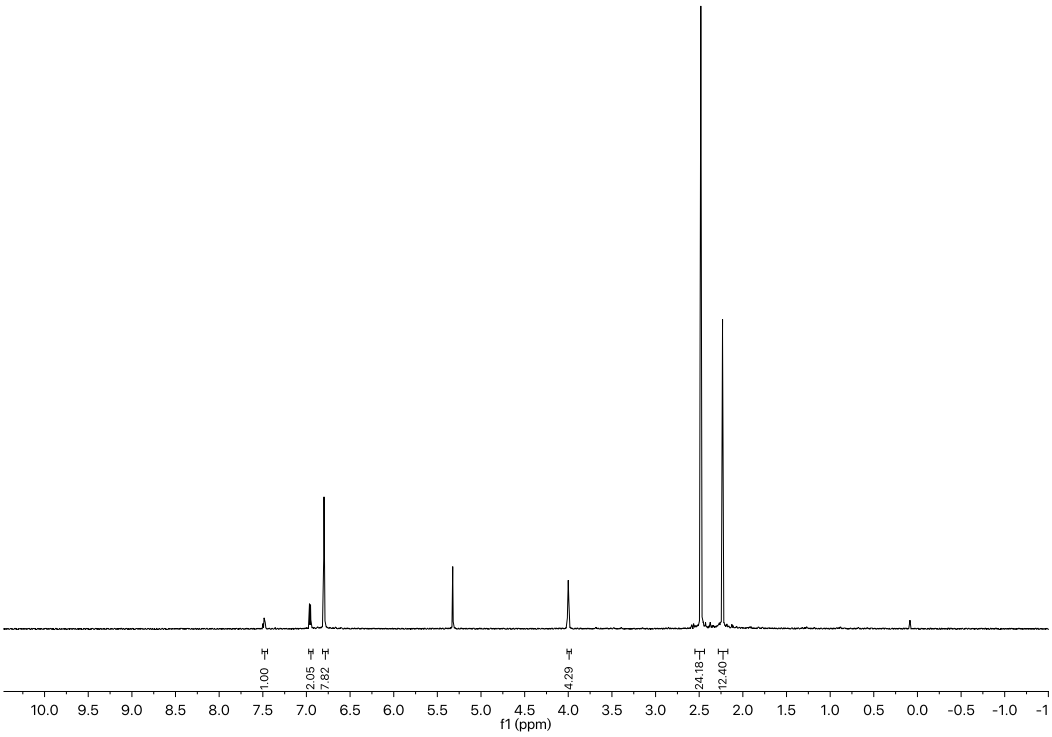

Figure S7. $_{1}$H NMR spectrum of ($_{Mes}$PNP)RhCl (**3a**) (dichloromethane-*d*$_2$, 600 MHz).

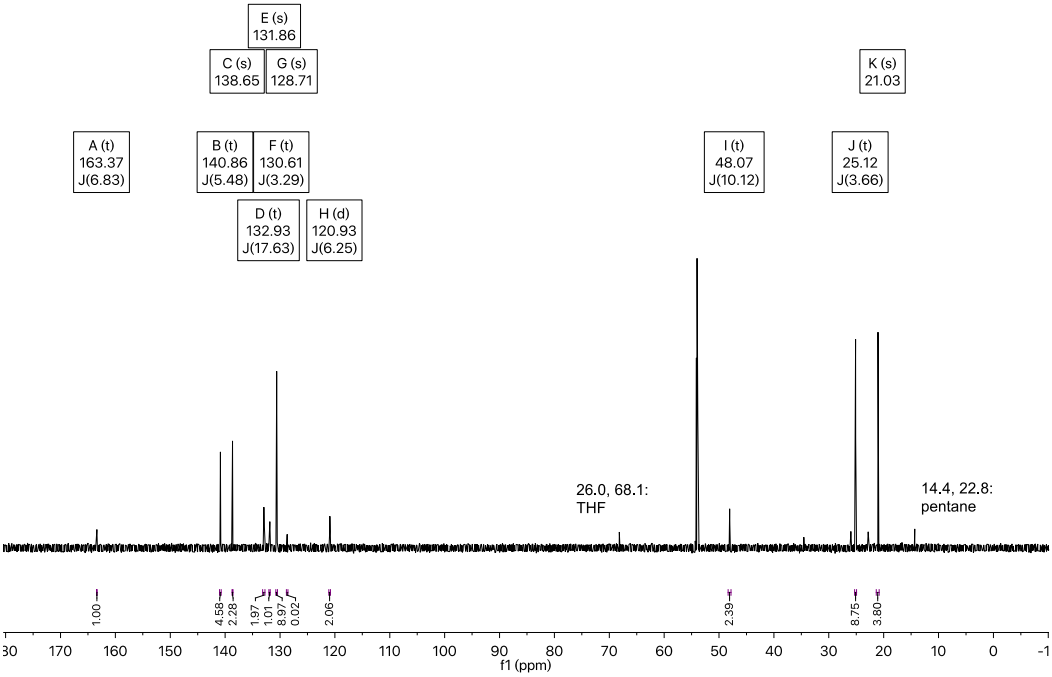

Figure S8. $_{13}$C{$_{1}$H} NMR spectrum of ($_{Mes}$PNP)RhCl (**3a**) (dichloromethane-*d*$_2$, 151 MHz).

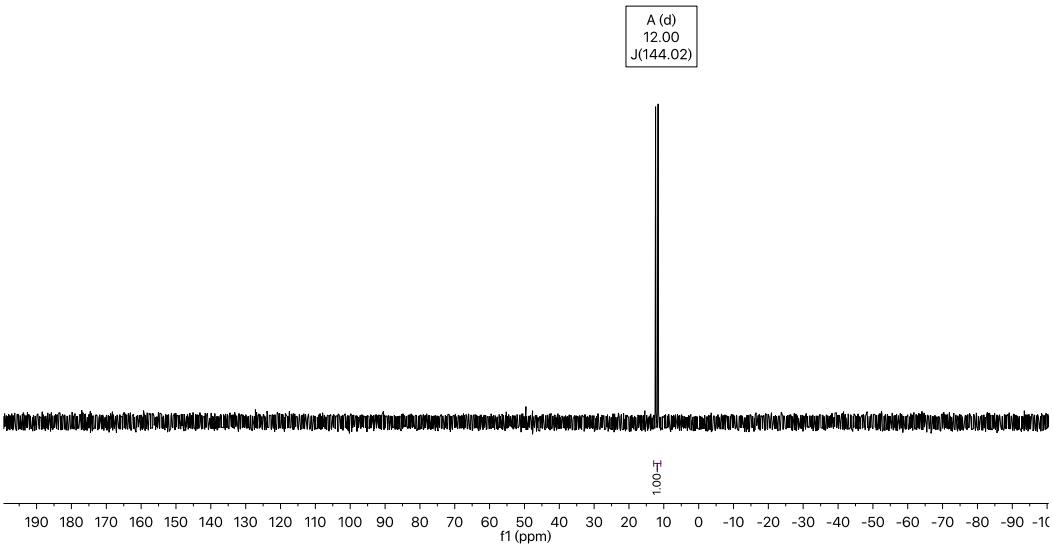

Figure S9. $^{31}P\{^{1}H\}$ NMR spectrum of (^{Mes}PNP)RhCl (**3a**) (dichloromethane-d_2, 202 MHz).

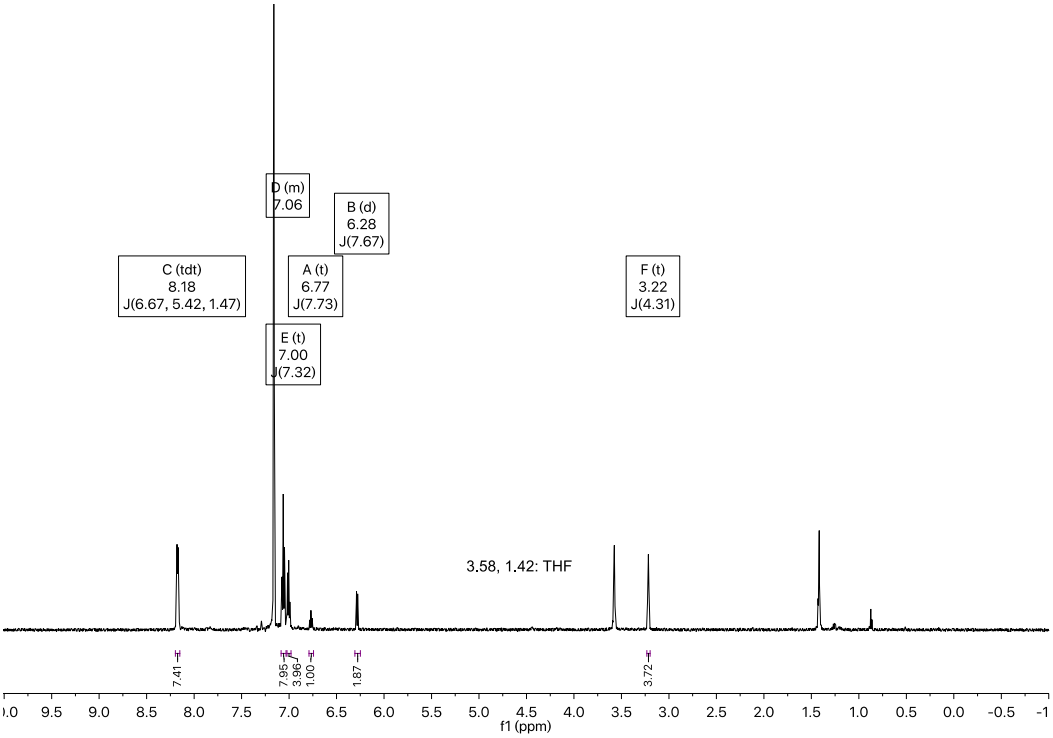

Figure S10. ^{1}H NMR spectrum of (^{Ph}PNP)RhCl (**4a**) (benzene-d_6, 600 MHz).

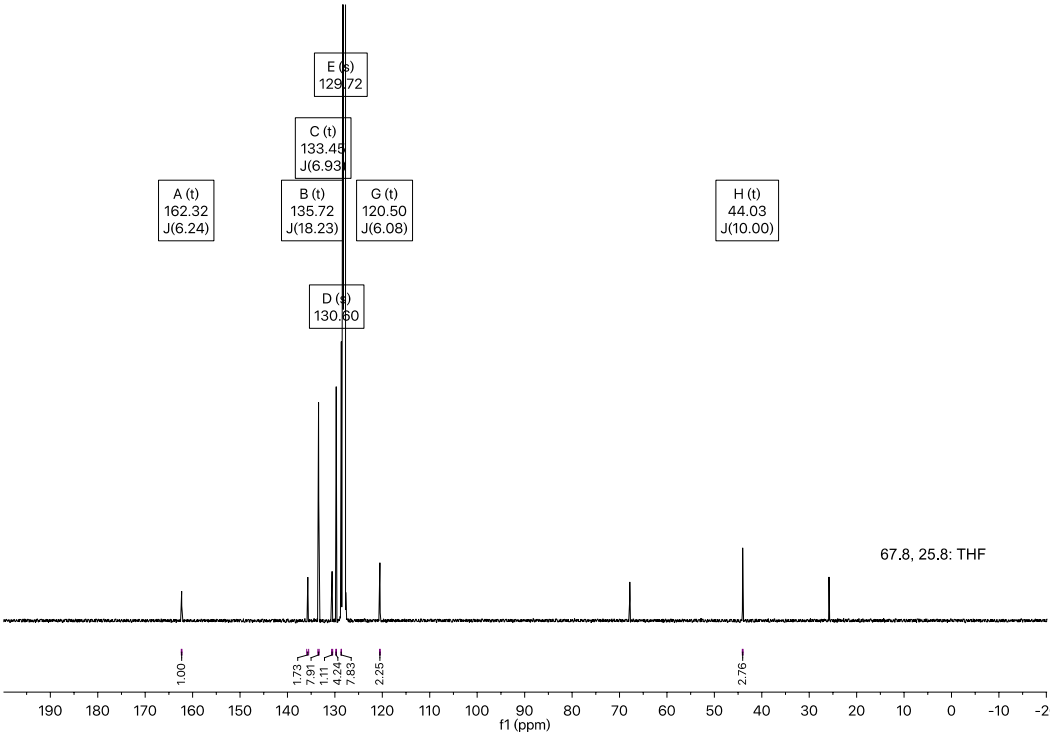

Figure S11. $^{13}C\{^{1}H\}$ NMR spectrum of (^{Ph}PNP)RhCl (**4a**) (benzene-d_6, 151 MHz).

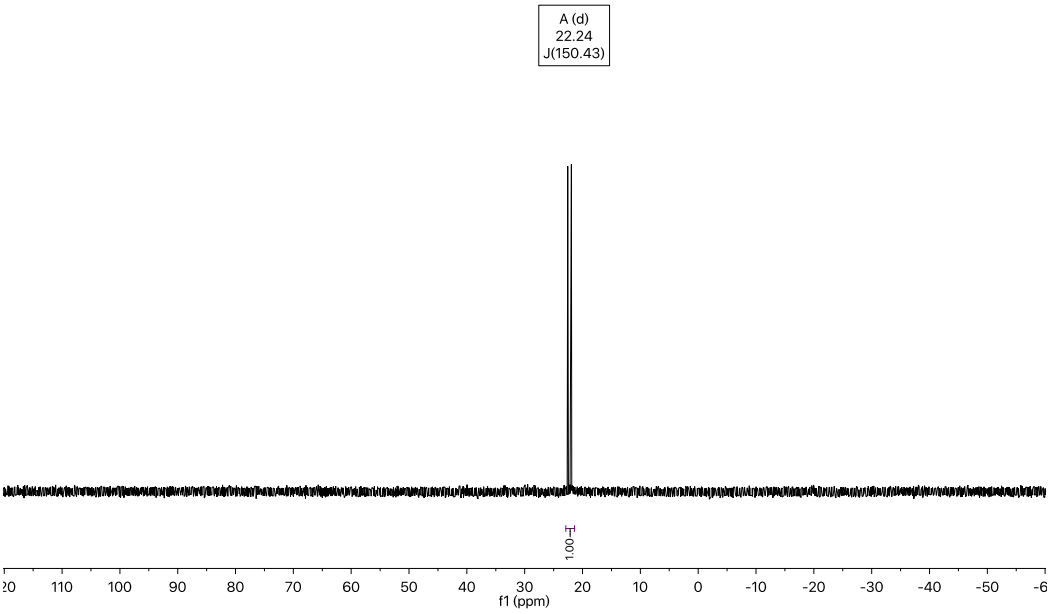

Figure S12. $^{31}P\{^{1}H\}$ NMR spectrum of (^{Ph}PNP)RhCl (**4a**) (benzene-d_6, 243 MHz).

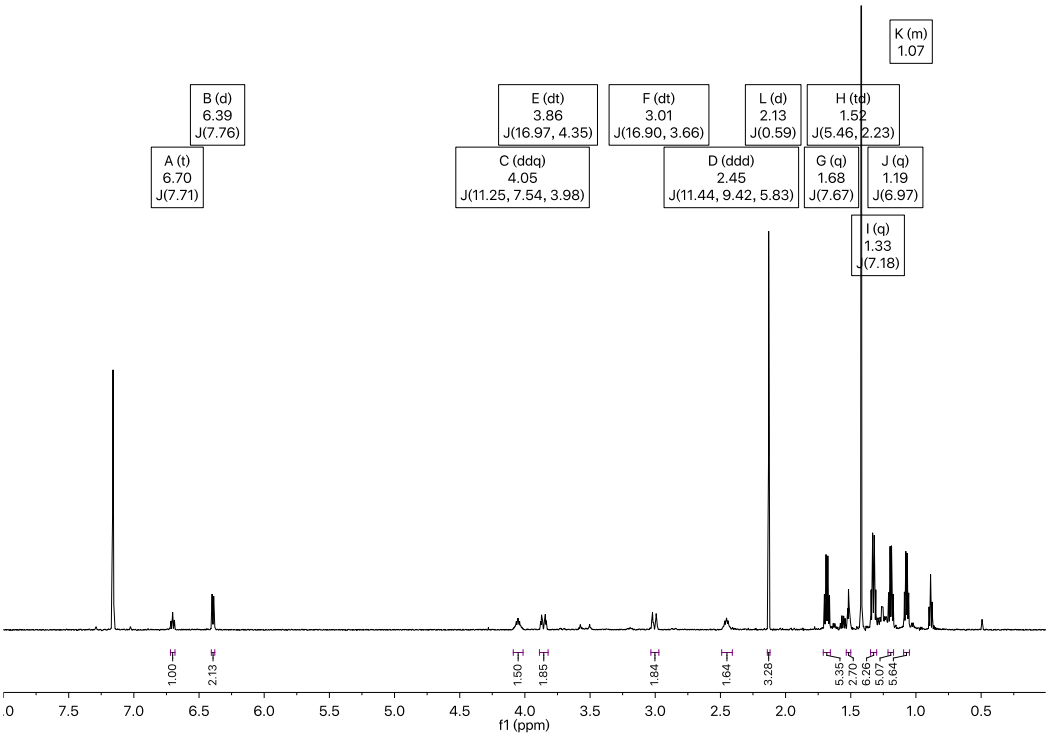

Figure S13. $_{1}$H NMR spectrum of ($_{iPr}$PNP)Rh(Me)(I)(Cl) (**2b-1** or **2b-2**) (benzene-d_6, 600 MHz).

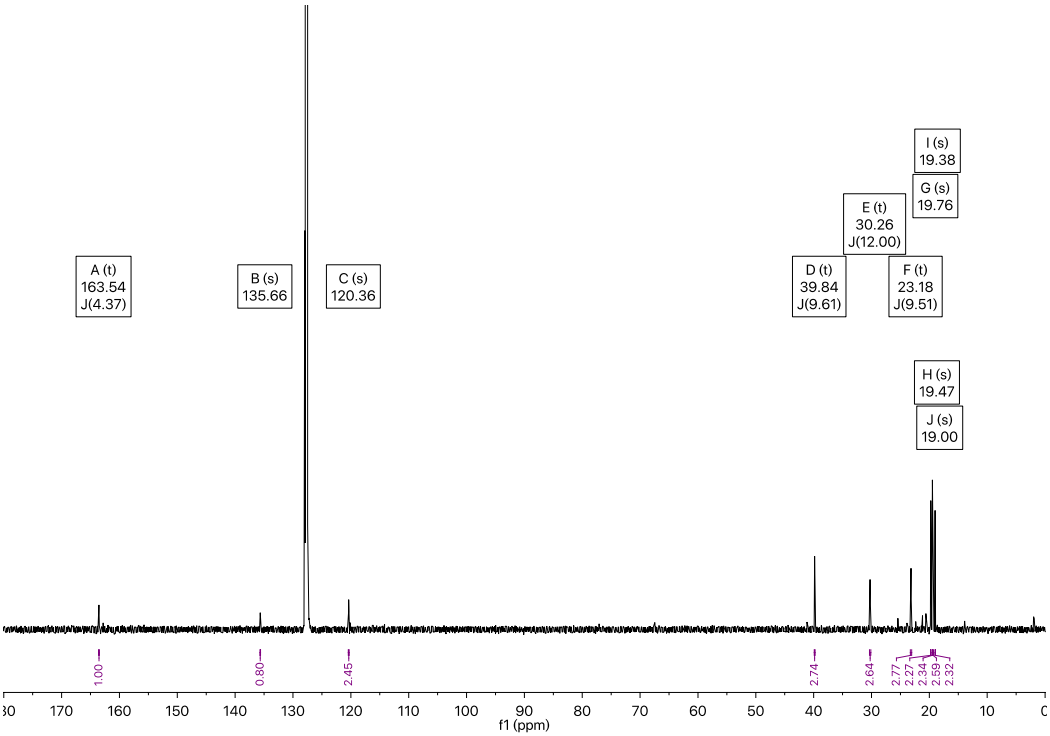

Figure S14. $_{13}$C{$_{1}$H} NMR spectrum of ($_{iPr}$PNP)Rh(Me)(I)(Cl) (**2b-1** or **2b-2**) (benzene-d_6, 151 MHz).

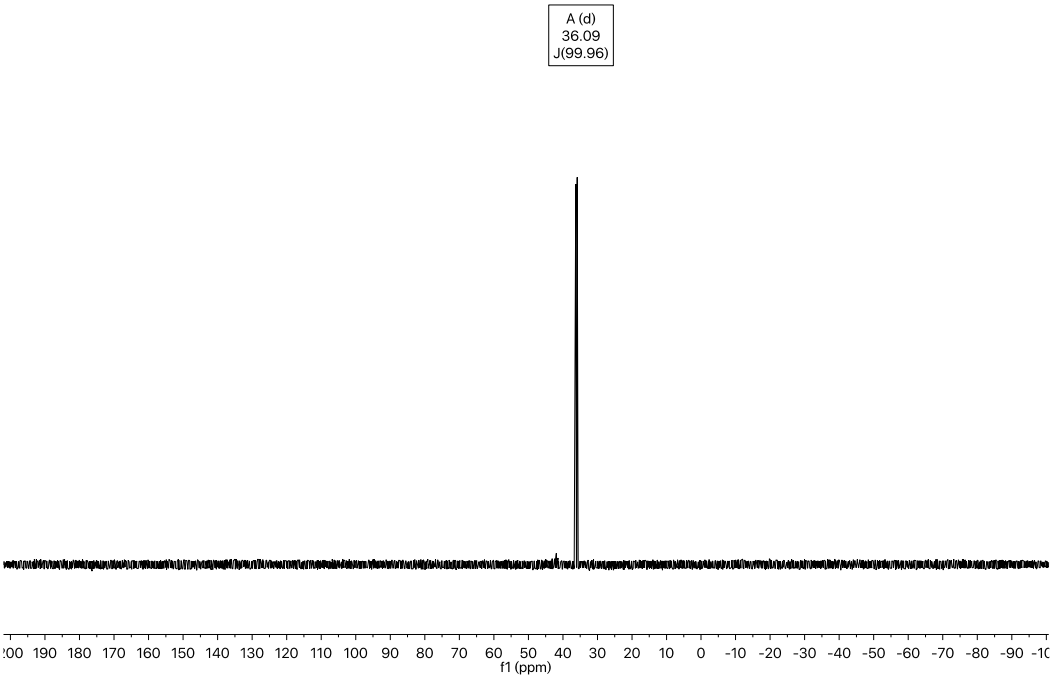

Figure S15. $^{31}P\{^{1}H\}$ NMR spectrum of (^{iPr}PNP)Rh(Me)(I)(Cl) (**2b-1** or **2b-2**) (benzene-d_6, 243 MHz).

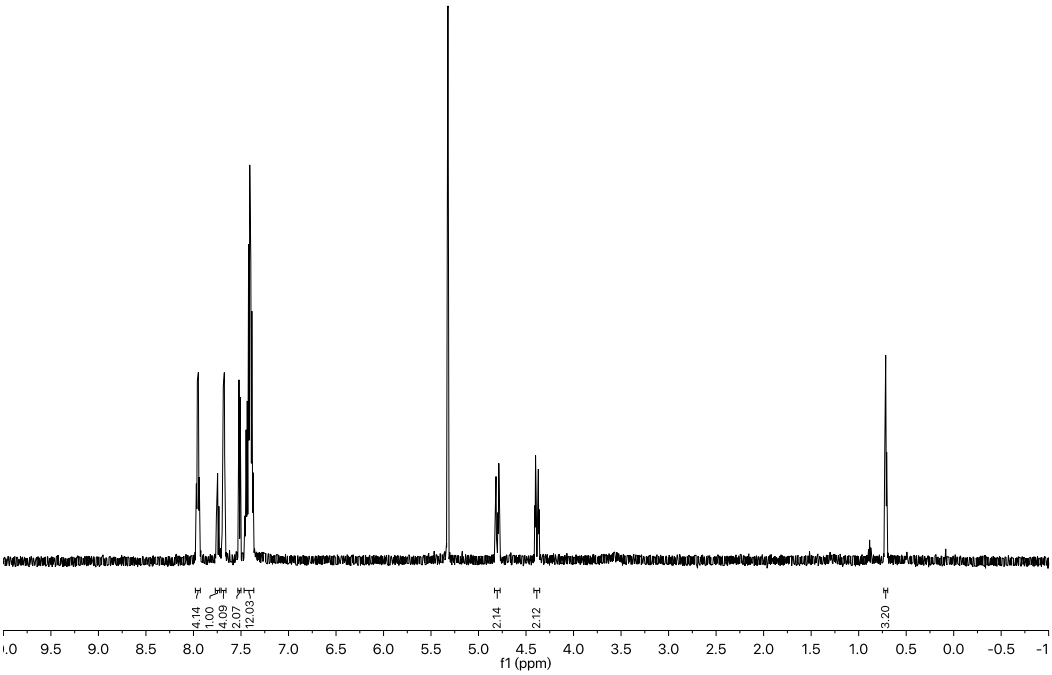

Figure S16. ^{1}H NMR spectrum of (^{Ph}PNP)Rh(Me)(I)(Cl) (**4b-1**) (dichloromethane-d_2, 600 MHz).

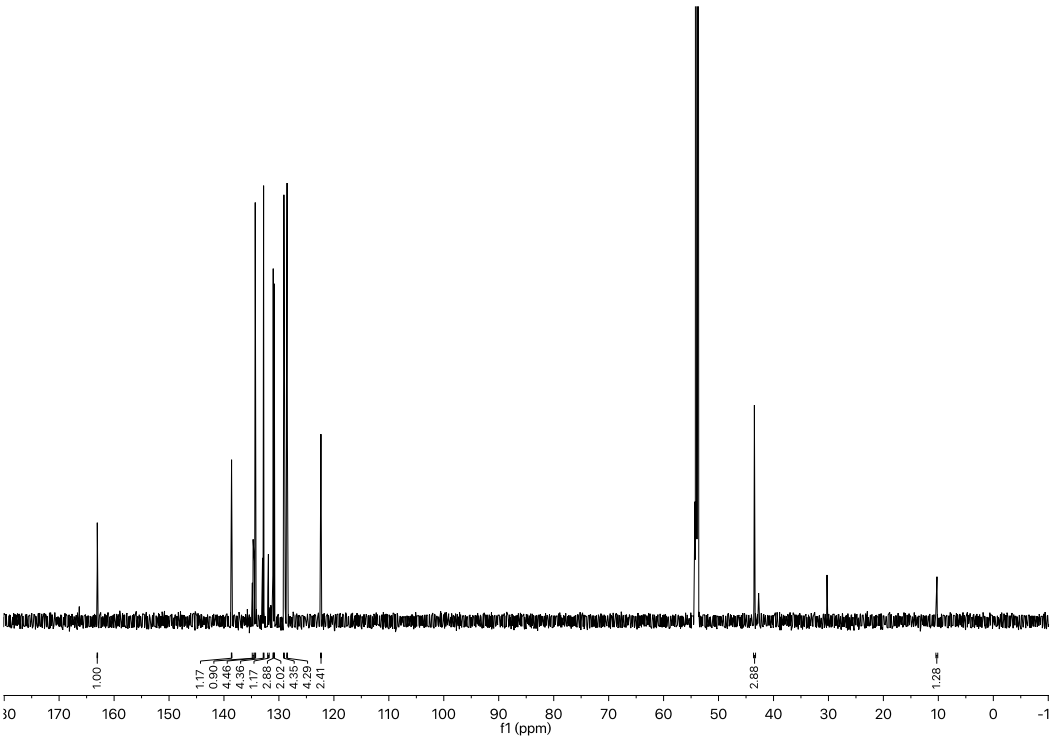

Figure S17. $^{13}C\{^{1}H\}$ NMR spectrum of (^{Ph}PNP)Rh(Me)(I)(Cl) (**4b-1**) (dichloromethane-d_2, 201 MHz).

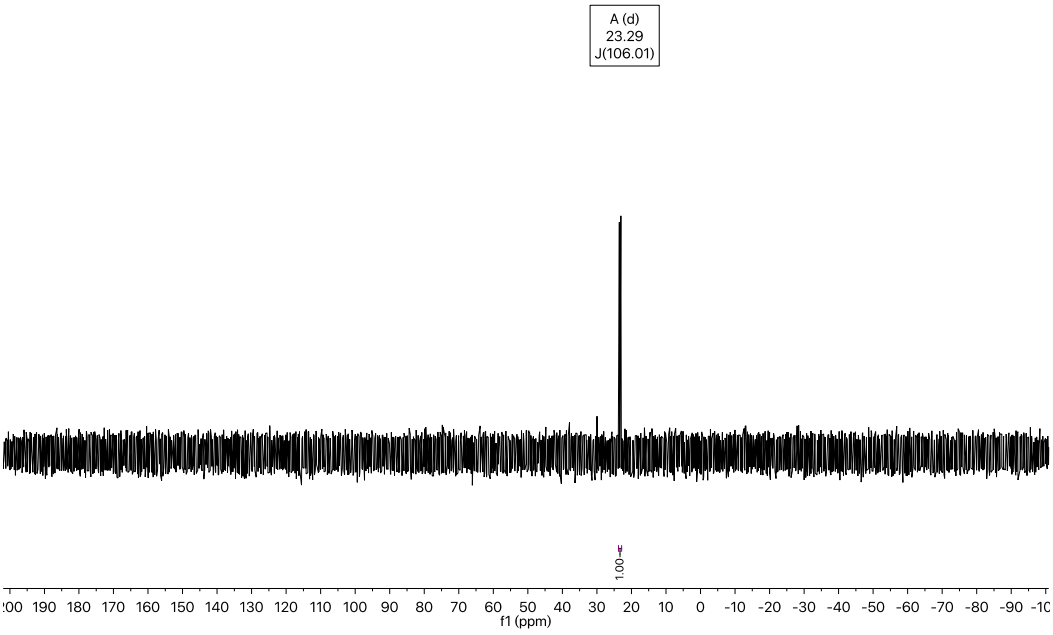

Figure S18. $^{31}P\{^{1}H\}$ NMR spectrum of (^{Ph}PNP)Rh(Me)(I)(Cl) (**4b-1**) (dichloromethane-d_2, 243 MHz).

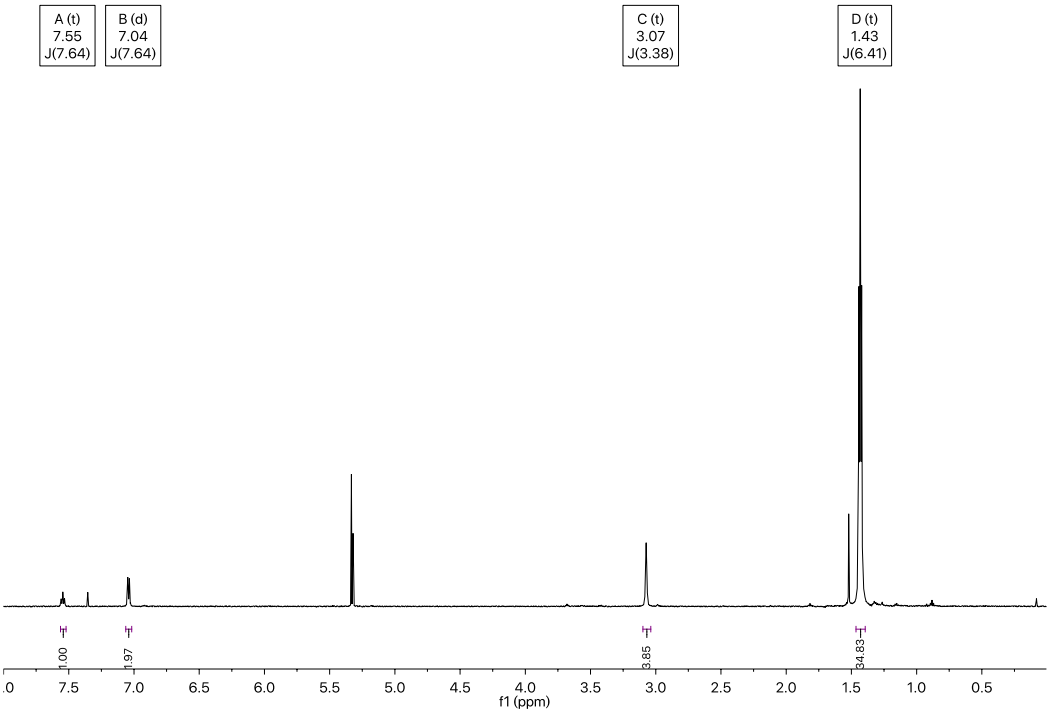

Figure S19. $_{1}$H NMR spectrum of ($_{tBu}$PNP)RhI (**1c**) (dichloromethane-d_2, 600 MHz).

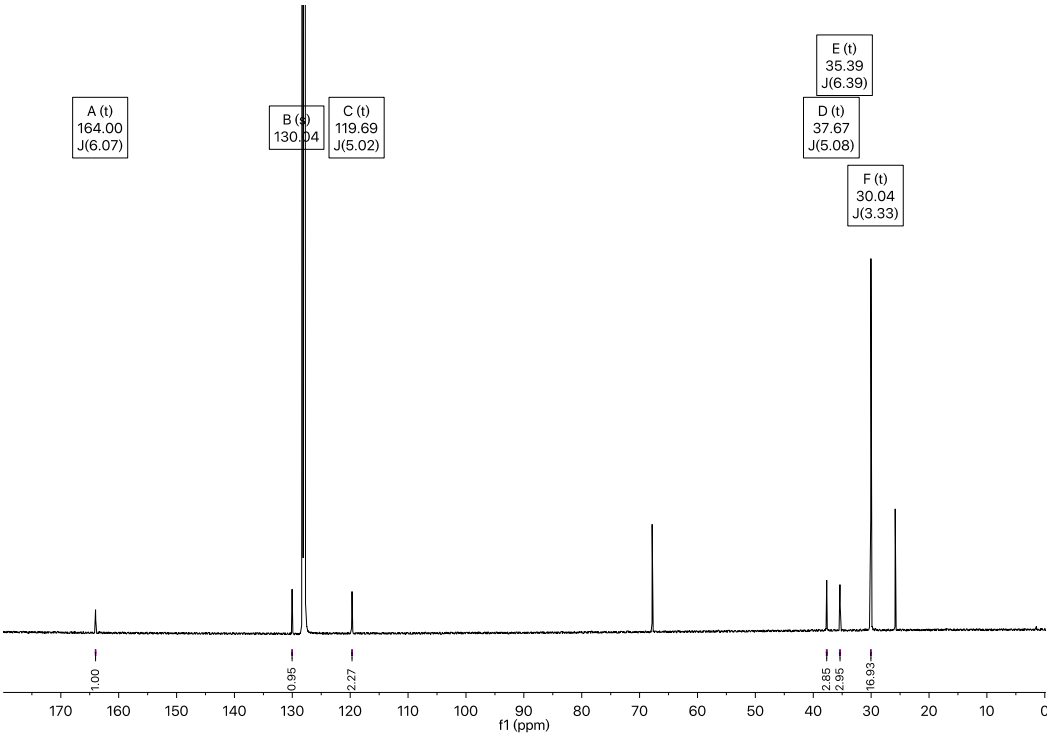

Figure S20. $_{13}$C{$_{1}$H} NMR spectrum of ($_{tBu}$PNP)RhI (**1c**) (benzene-d_6, 151 MHz).

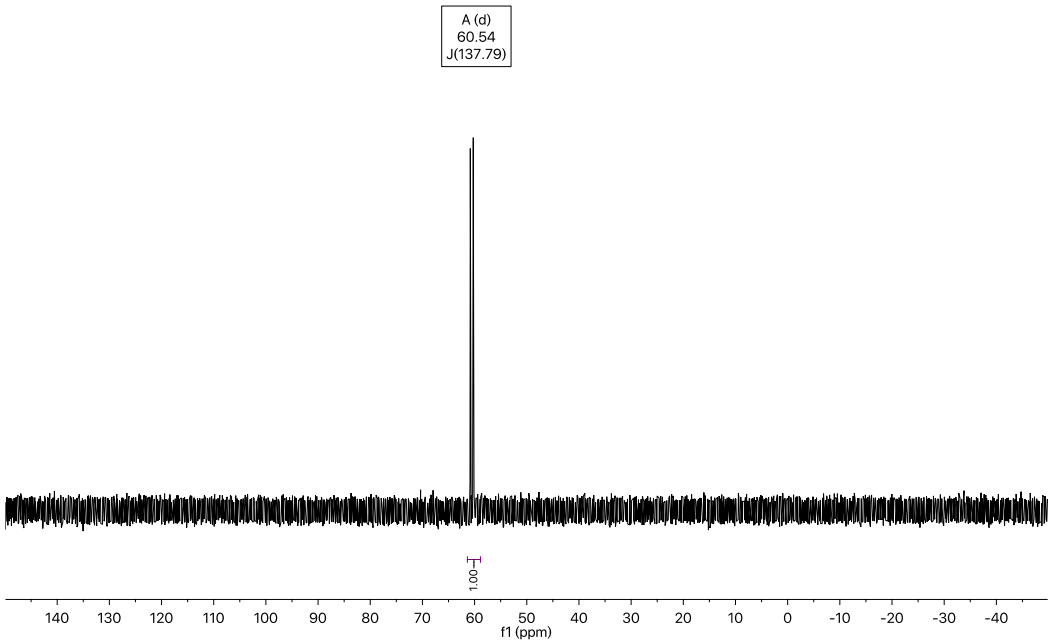

Figure S21. $^{31}P\{^{1}H\}$ NMR spectrum of (^{tBu}PNP)RhI (**1c**) (dichloromethane-d_2, 243 MHz).

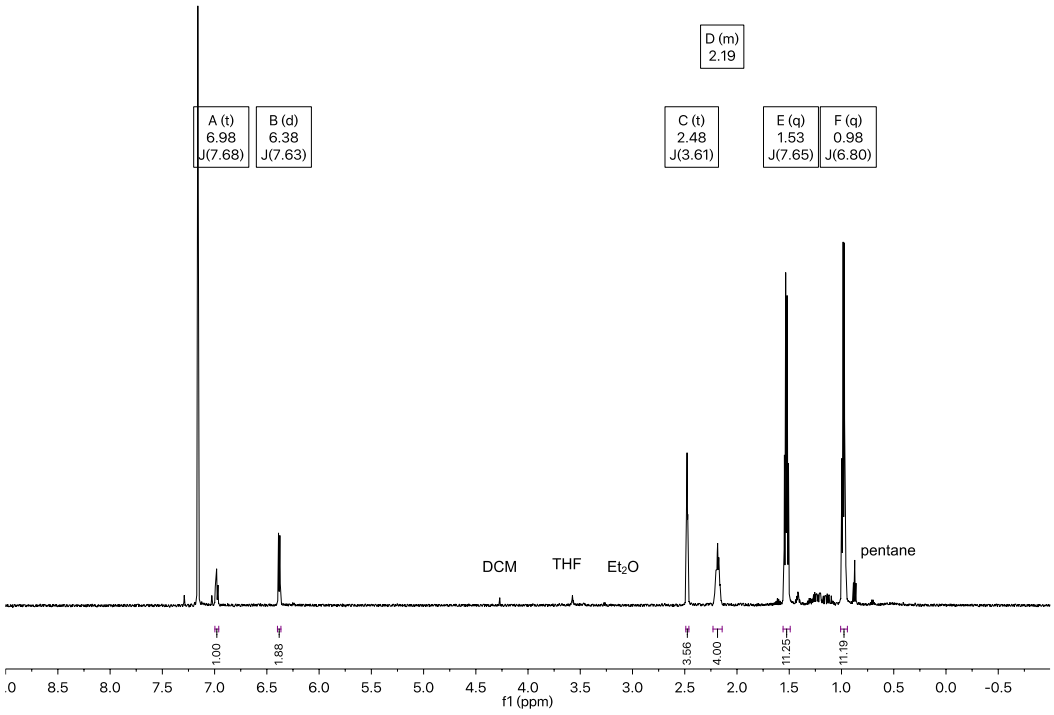

Figure S22. ^{1}H NMR spectrum of (^{iPr}PNP)RhI (**2c**) (benzene-d_6, 600 MHz).

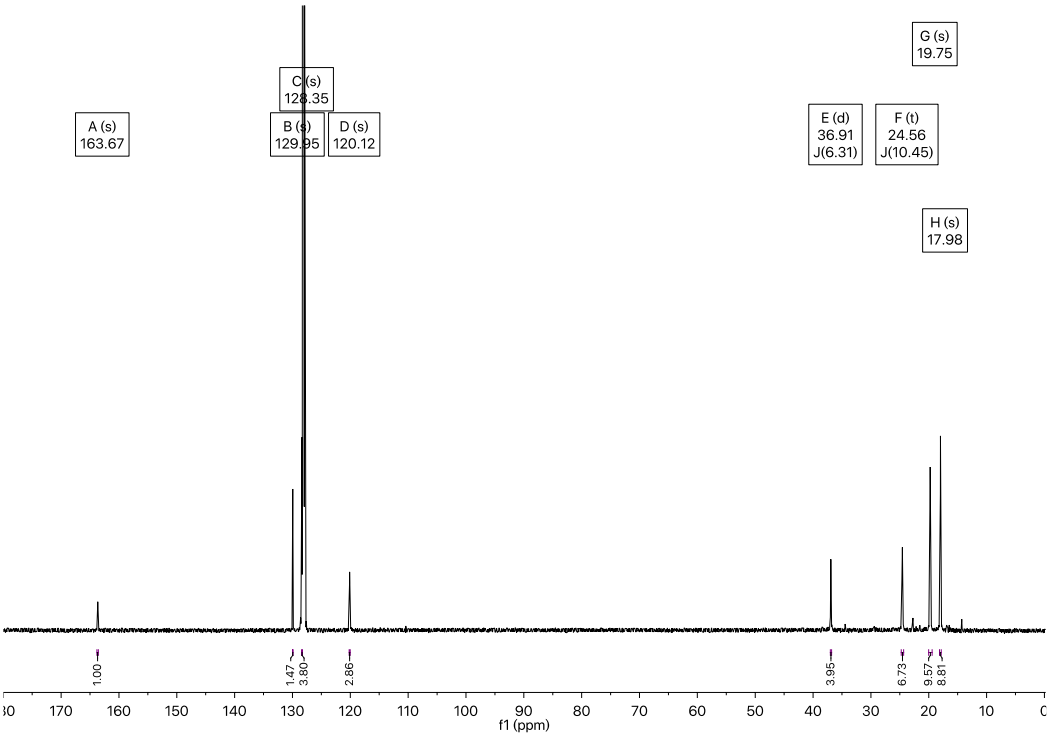

Figure S23. $^{13}C\{^{1}H\}$ NMR spectrum of (^{iPr}PNP)RhI (**2c**) (benzene-d_6, 151 MHz).

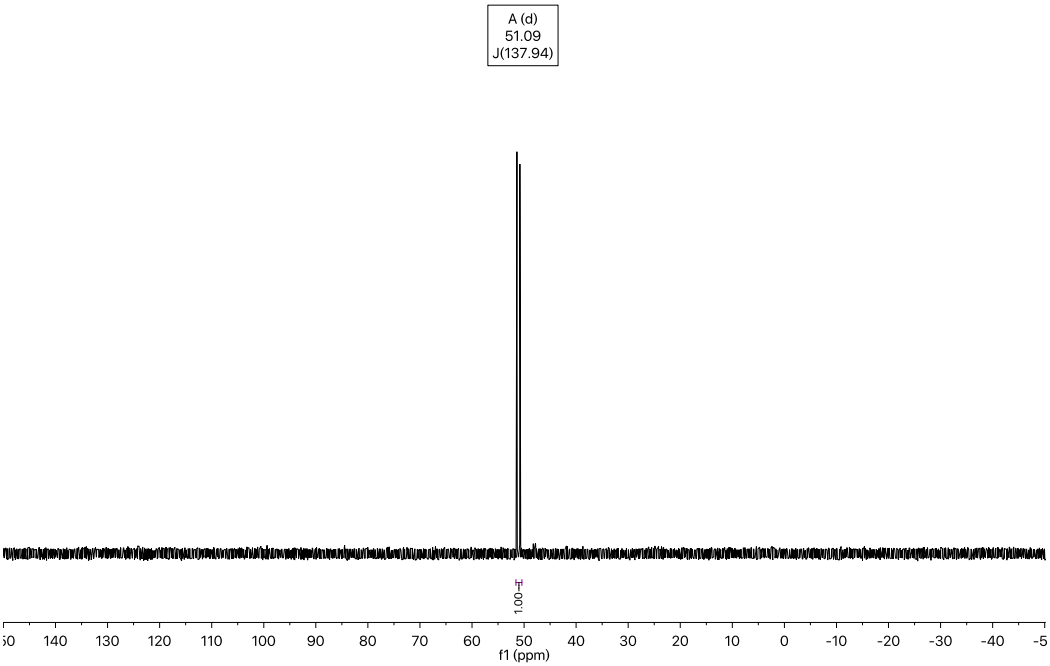

Figure S24. $^{31}P\{^{1}H\}$ NMR spectrum of (^{iPr}PNP)RhI (**2c**) (benzene-d_6, 243 MHz).

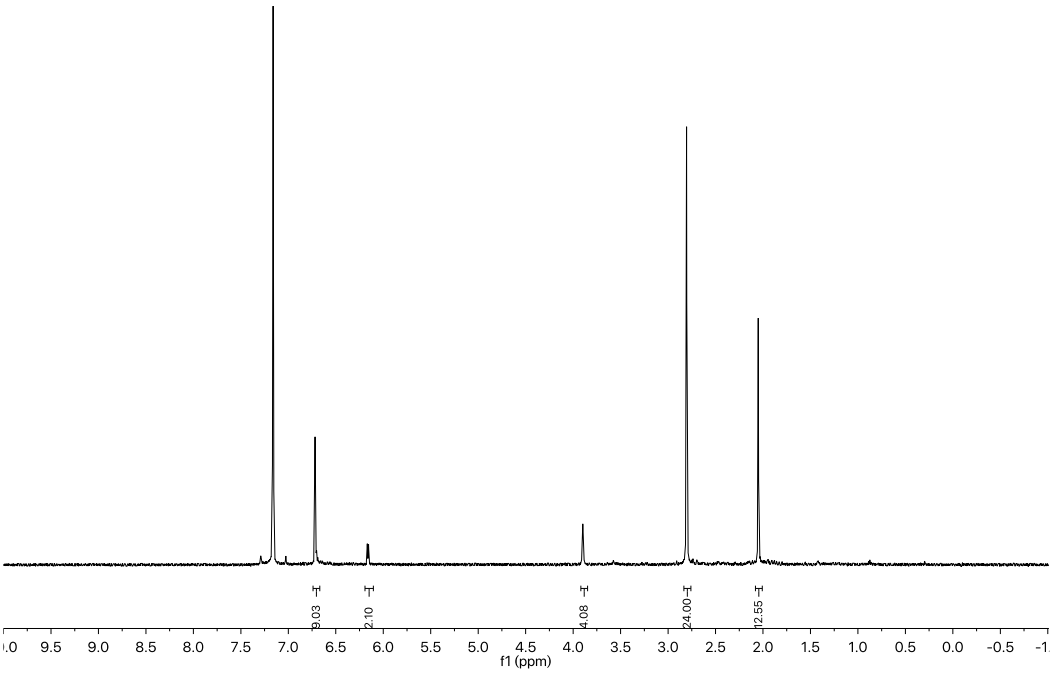

Figure S25. $_{1}$H NMR spectrum of ($_{Mes}$PNP)RhI (**3c**) (benzene-d_6, 600 MHz).

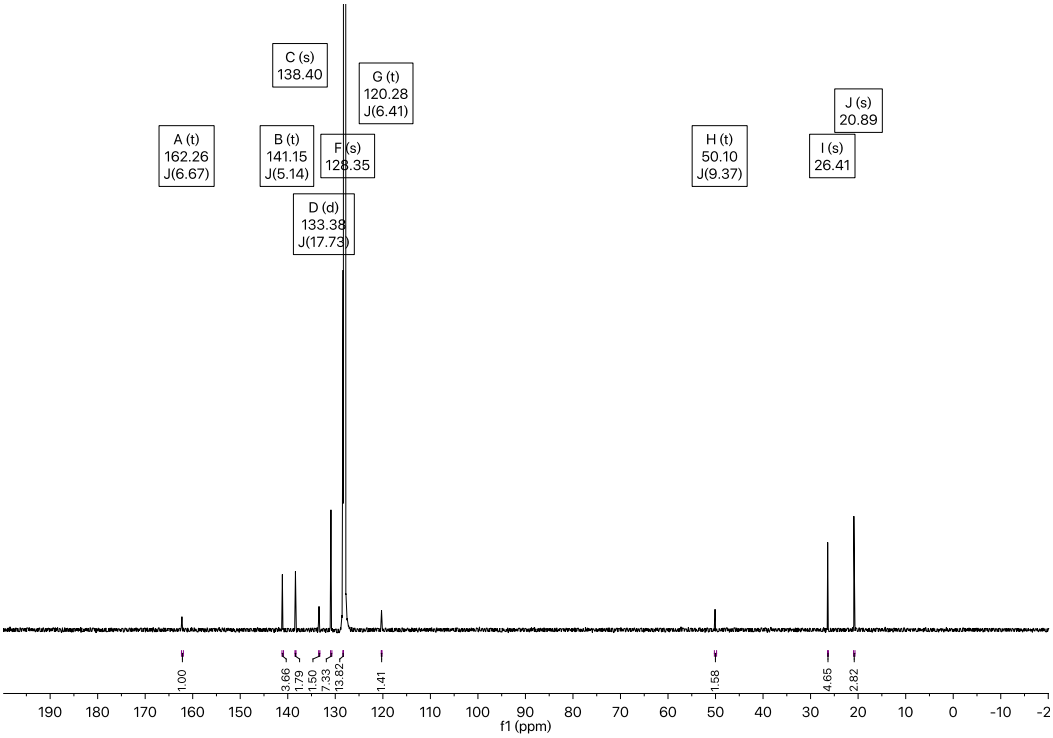

Figure S26. $_{13}$C{$_{1}$H} NMR spectrum of ($_{Mes}$PNP)RhI (**3c**) (benzene-d_6, 201 MHz).

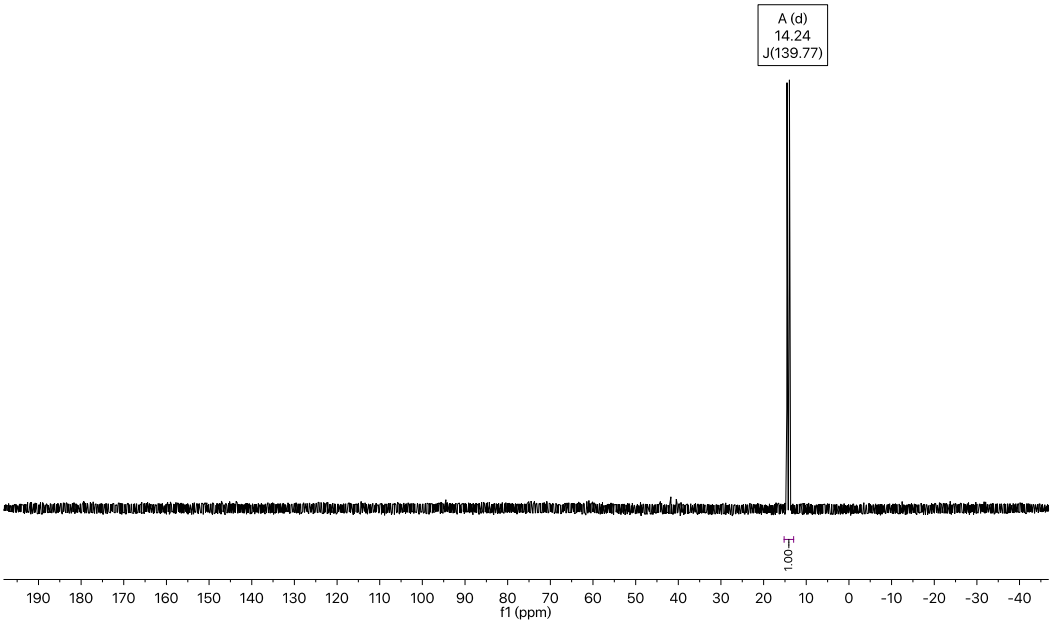

Figure S27. $^{31}P\{^{1}H\}$ NMR spectrum of (^{Mes}PNP)RhI (**3c**) (benzene-d_6, 243 MHz).

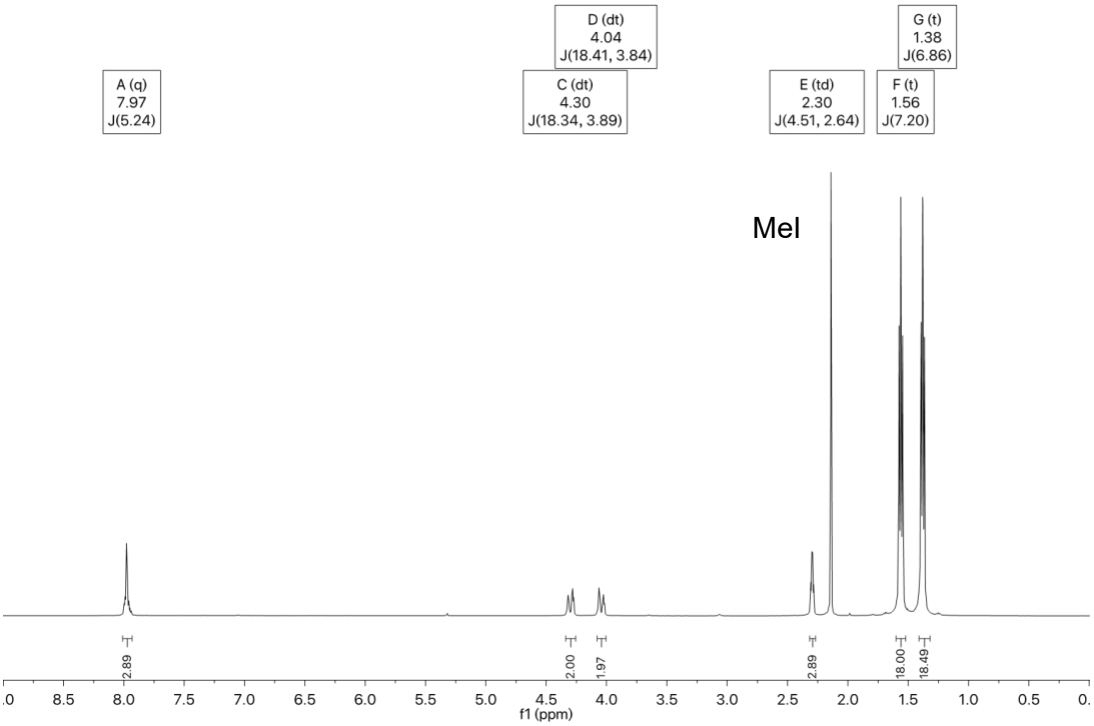

Figure S28. ^{1}H NMR spectrum of [(^{tBu}PNP)Rh(Me)(I)](I) (**1d'**) (dichloromethane-d_2, 600 MHz).

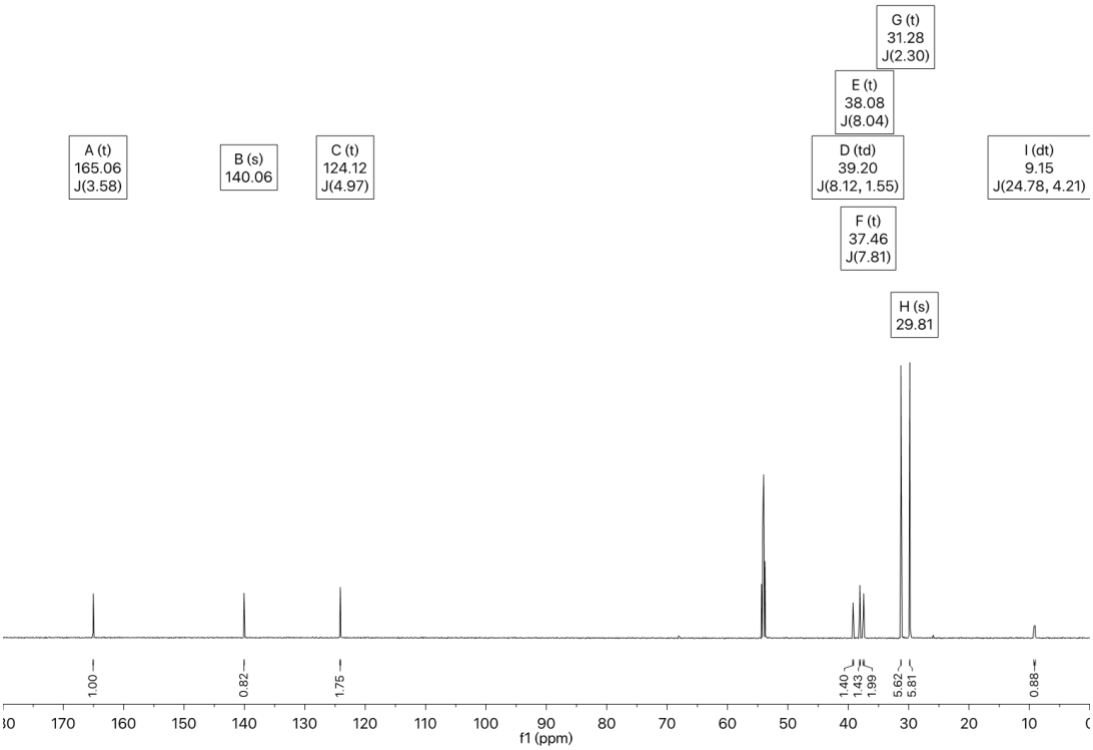

Figure S29. $^{13}C\{^{1}H\}$ NMR spectrum of [(^{tBu}PNP)Rh(Me)(I)](I) (**1d'**) (dichloromethane-d_2, 151 MHz).

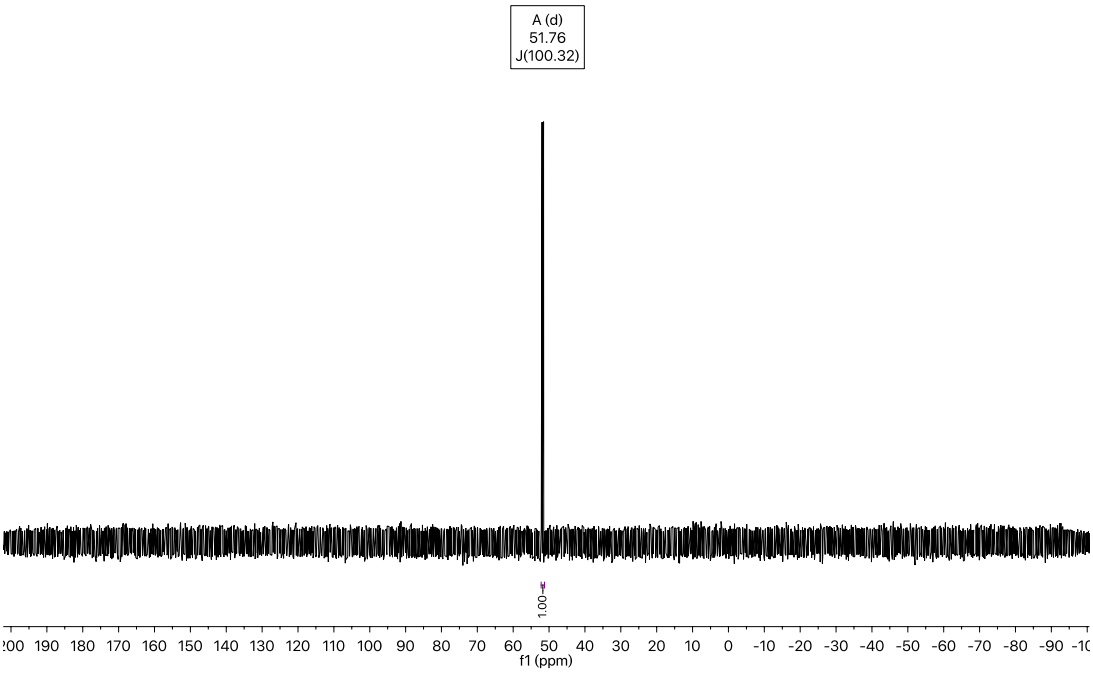

Figure S30. $^{31}P\{^{1}H\}$ NMR spectrum of [(^{tBu}PNP)Rh(Me)(I)](I) (**1d'**) (dichloromethane-d_2, 243 MHz).

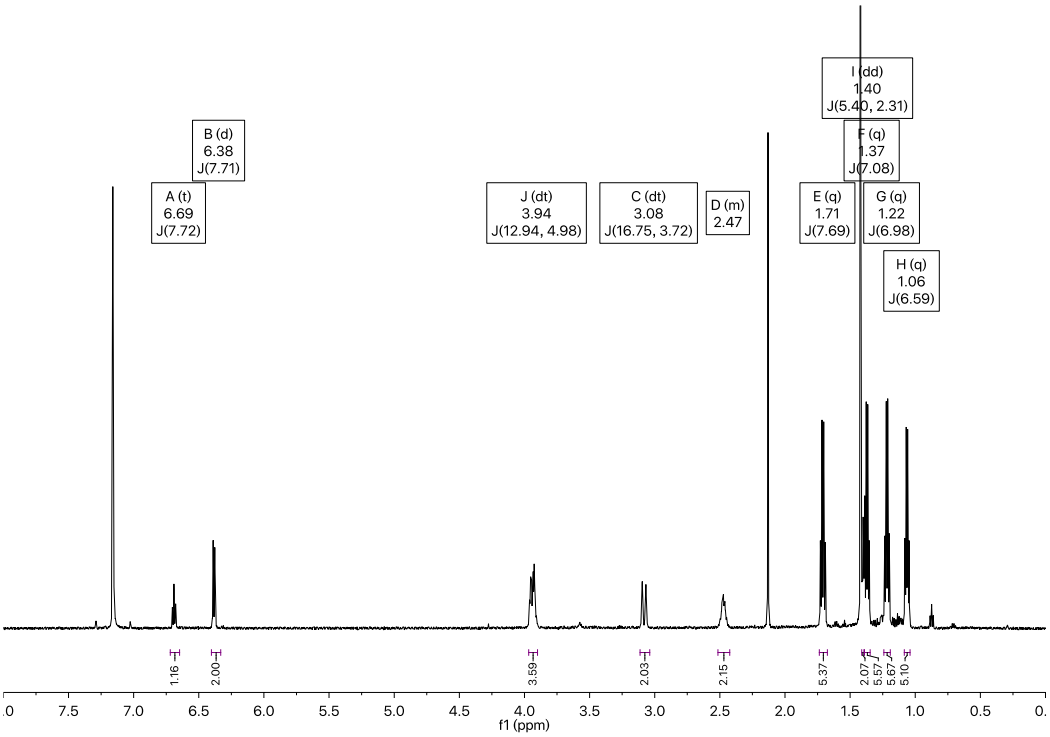

Figure S31. $_{1}$H NMR spectrum of *cis*-($_{iPr}$PNP)Rh(Me)(I)$_{2}$ (**2d**) (benzene-*d*$_{6}$, 600 MHz).

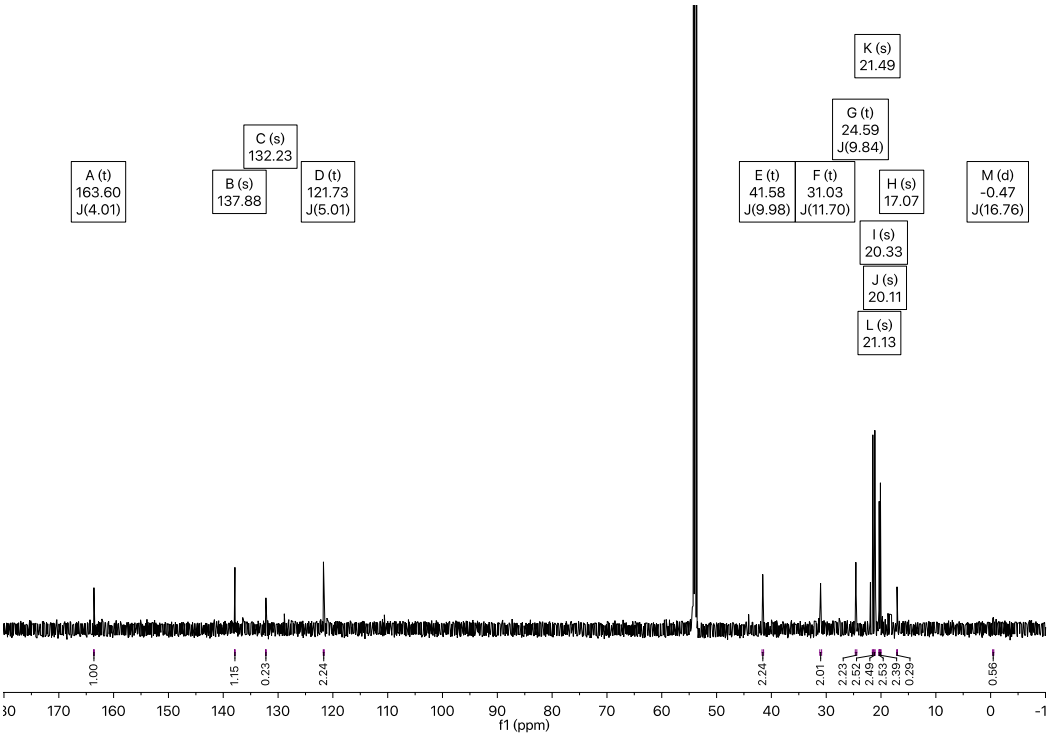

Figure S32. $_{13}$C{$_{1}$H} NMR spectrum of *cis*-($_{iPr}$PNP)Rh(Me)(I)$_{2}$ (**2d**) (dichloromethane-*d*$_{2}$, 151 MHz).

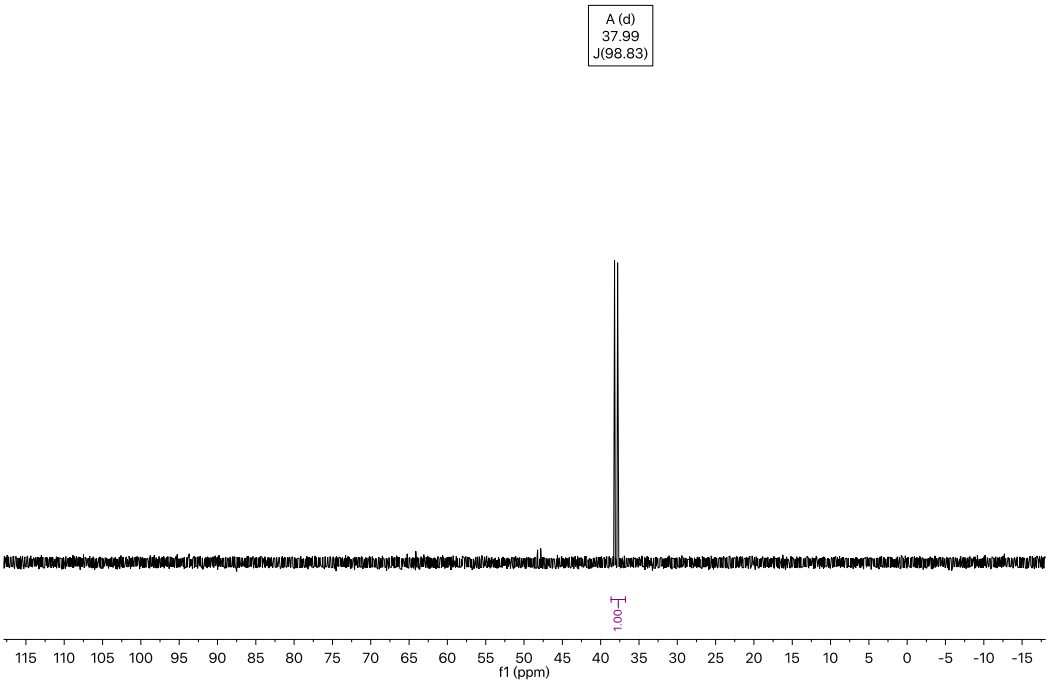

Figure S33. $^{31}P\{^{1}H\}$ NMR spectrum of *cis*-(^{iPr}PNP)Rh(Me)(I)$_2$ (**2d**) (benzene-d_6, 243 MHz).

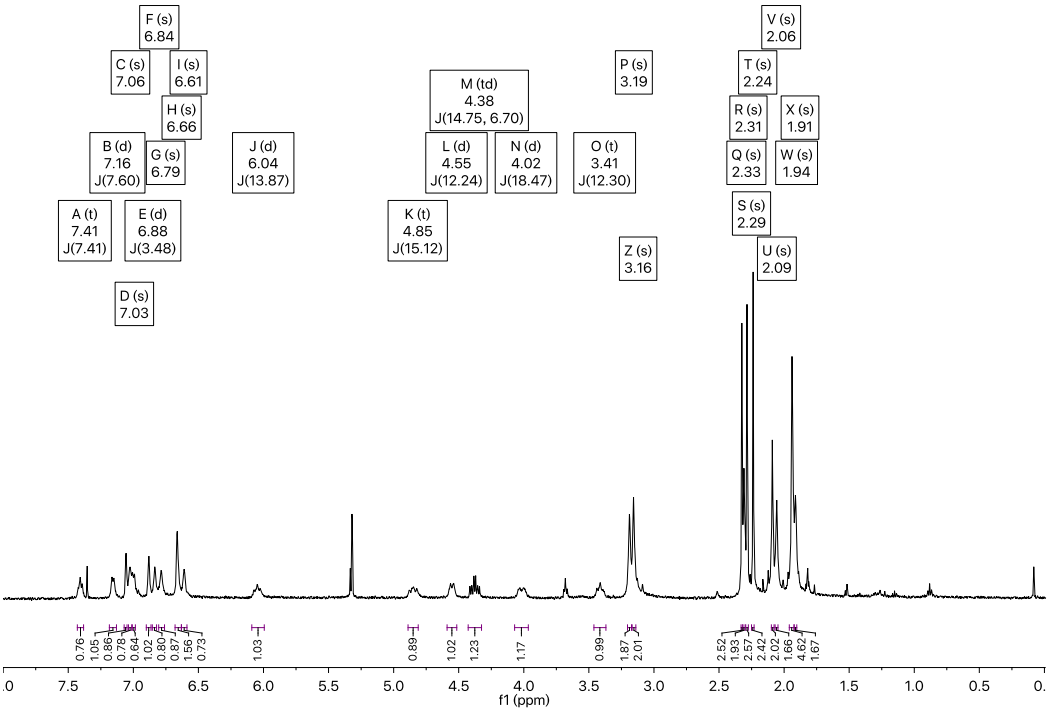

Figure S34. ^{1}H NMR spectrum of (^{Mes}PNP*)Rh(I)$_2$ (**3d''**) (dichloromethane-d_2, 500 MHz).

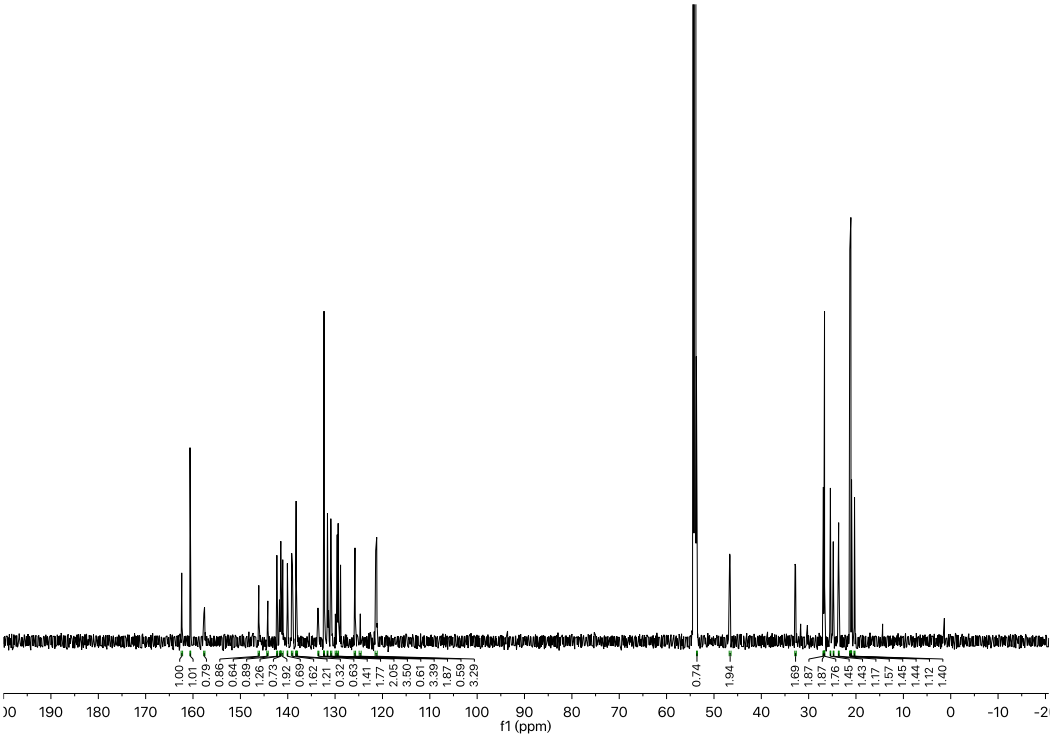

Figure S35. $^{13}C\{^{1}H\}$ NMR spectrum of ($_{Mes}$PNP*)Rh(I)$_2$ (**3d"**) (dichloromethane-d_2, 201 MHz).

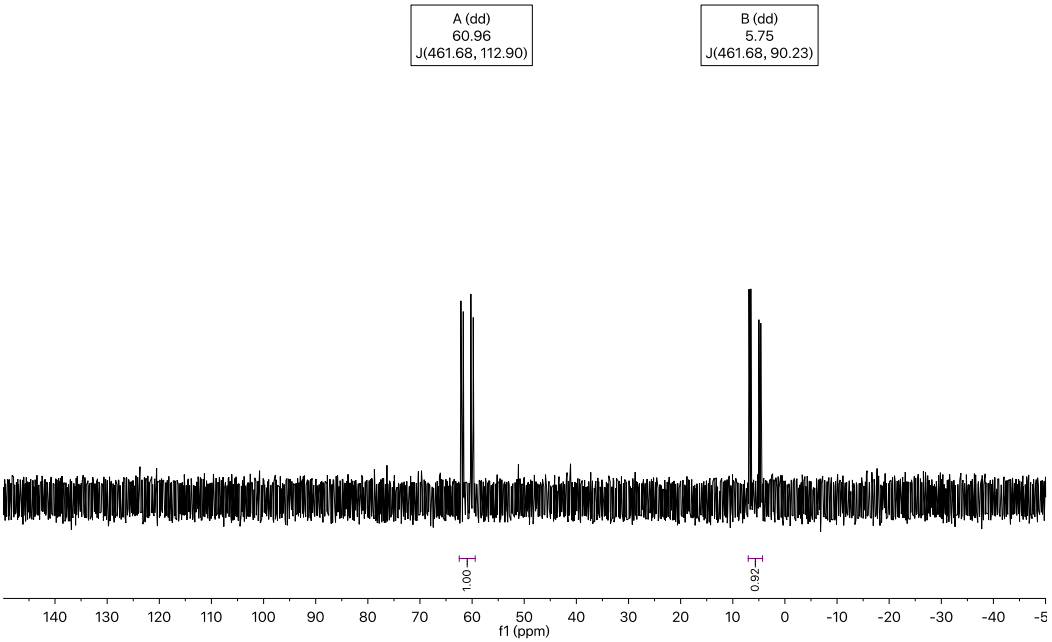

Figure S36. $^{31}P\{^{1}H\}$ NMR spectrum of ($_{Mes}$PNP*)Rh(I)$_2$ (**3d"**) (dichloromethane-d_2, 243 MHz).

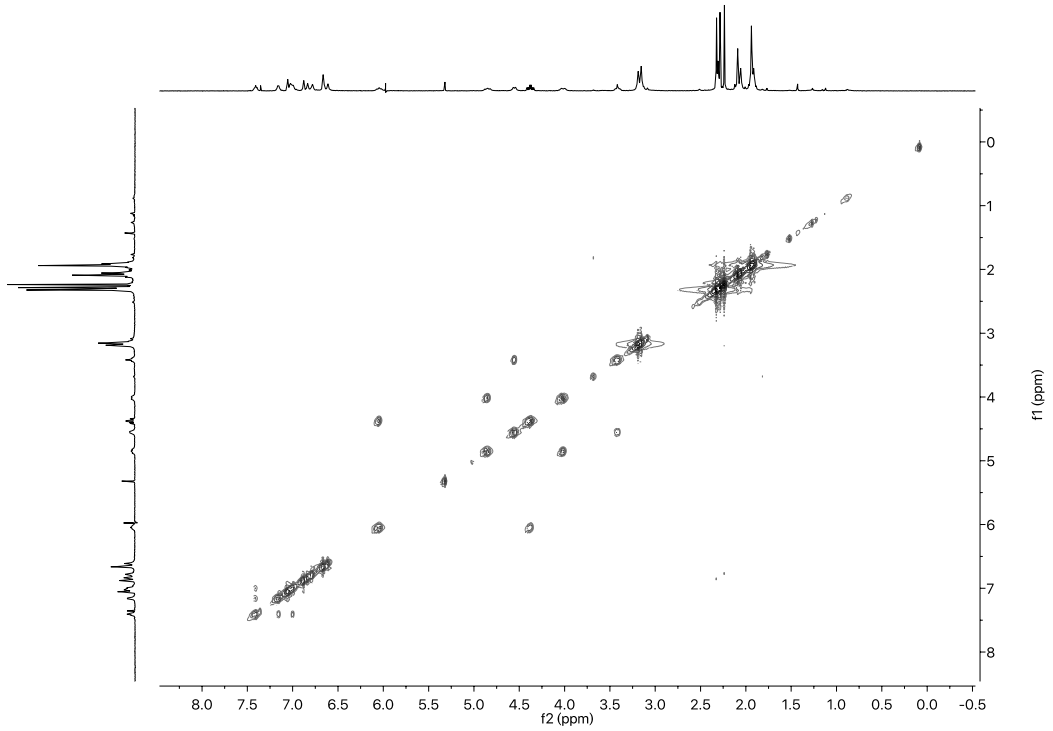

Figure S37. COSY of ($_{Mes}$PNP*)Rh(I)$_2$ (**3d"**) (dichloromethane-d_2, 800 MHz).

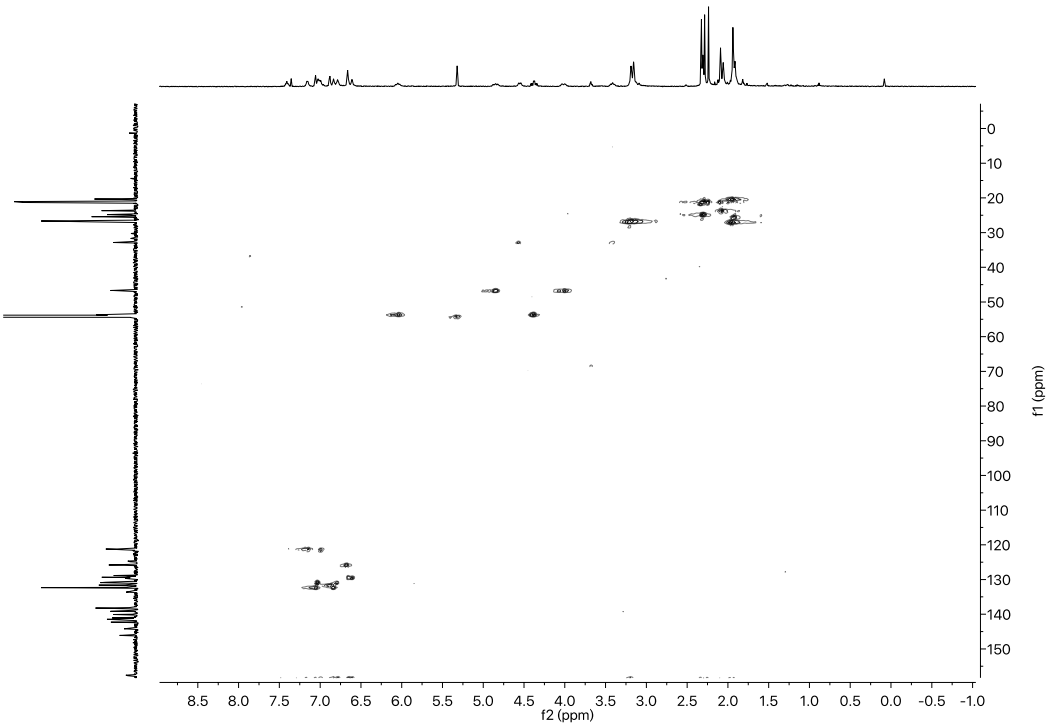

Figure S38. HSQC of ($_{Mes}$PNP*)Rh(I)$_2$ (**3d"**) (dichloromethane-d_2).

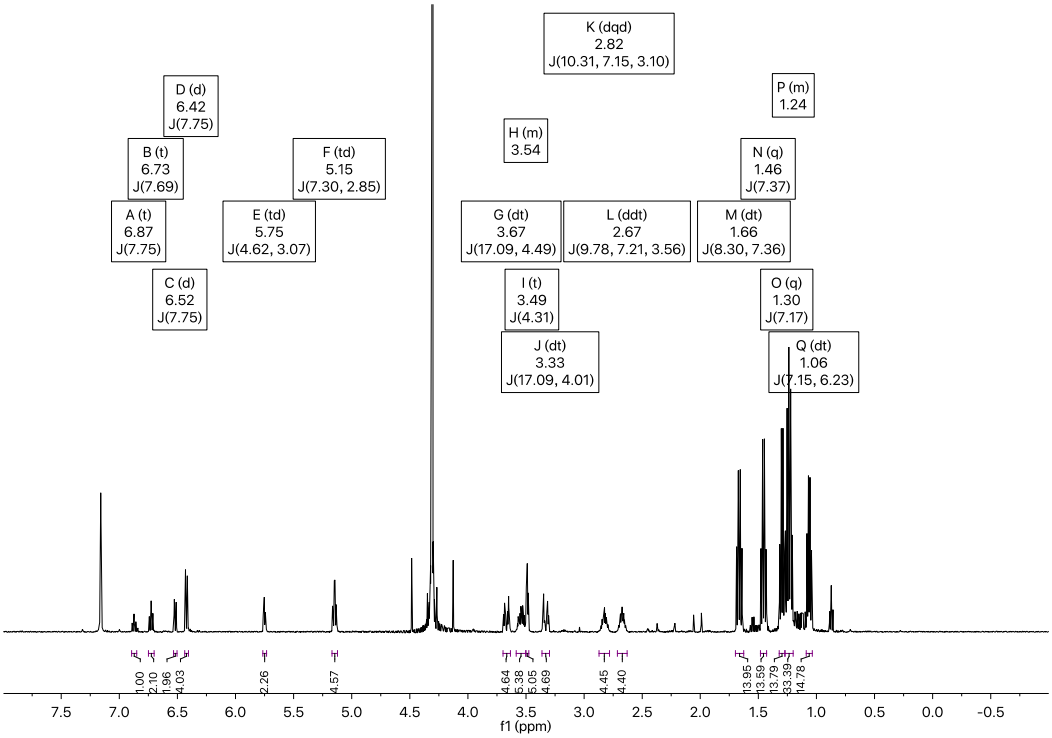

Figure S39. $_{1}$H NMR spectrum of ($_{iPr}$PNP)Rh(CH_2Cl)(Cl)$_2$ (**2e-*trans*** and **2e-*cis***) (benzene-d_6, 600 MHz). Peak A, C, E, H, I and P belong to *trans*-isomer. The remaining peaks belong to *cis*-isomer.

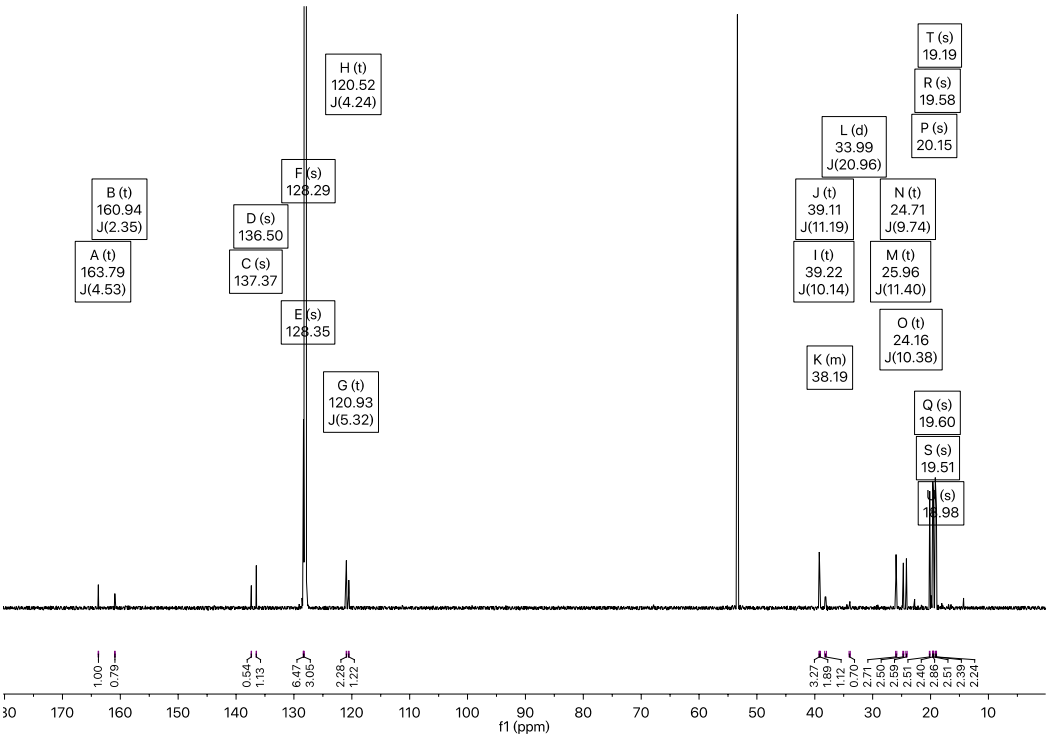

Figure S40. $_{13}$C{$_{1}$H} NMR spectrum of ($_{iPr}$PNP)Rh(CH_2Cl)(Cl)$_2$ (**2e-*trans*** and **2e-*cis***) (benzene-d_6, 151 MHz).

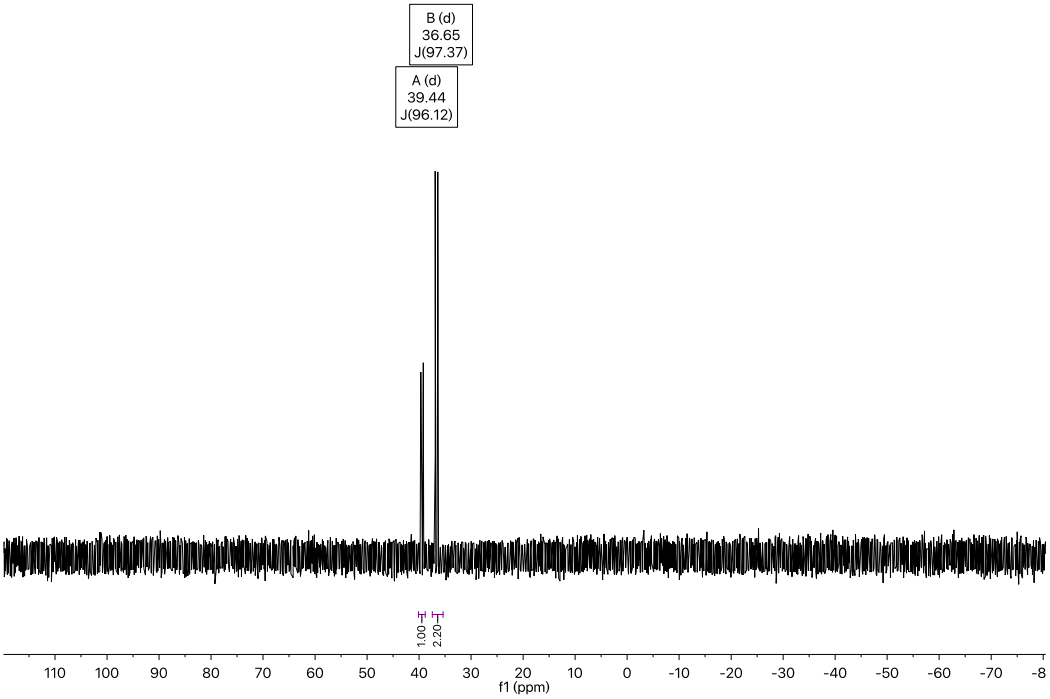

Figure S41. $^{31}P\{^{1}H\}$ NMR spectrum of (^{iPr}PNP)Rh(CH_2Cl)(Cl)$_2$ (**2e-*trans*** and **2e-*cis***) (benzene-d_6, 243 MHz).

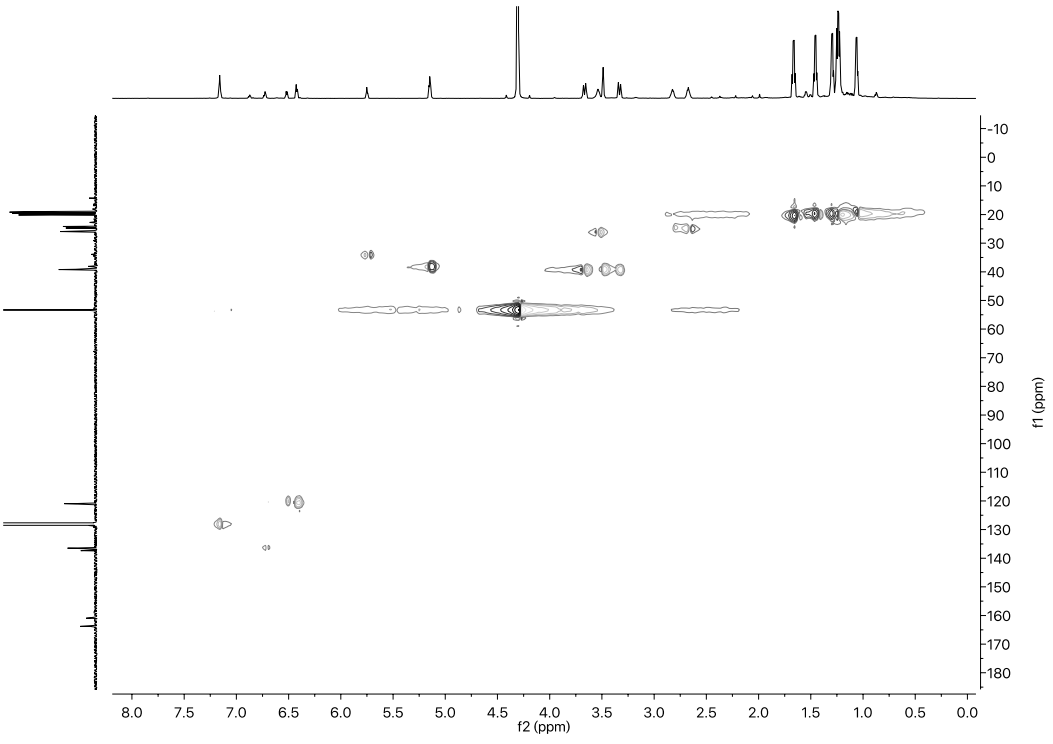

Figure S42. HSQC of (^{iPr}PNP)Rh(CH_2Cl)(Cl)$_2$ (**2e-*trans*** and **2e-*cis***) (benzene-d_6).

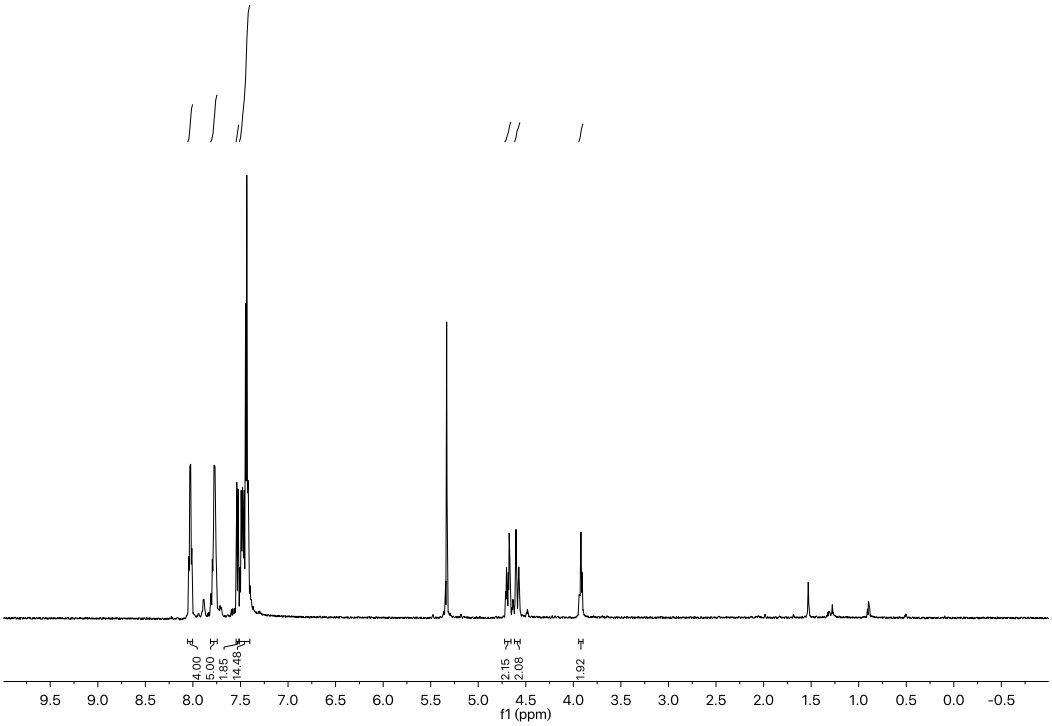

Figure S43. $_{1}$H NMR spectrum of *cis*-($_{Ph}$PNP)Rh(CH_2Cl)(Cl)$_2$ (**4e-*cis***) in dichloromethane-d_2.

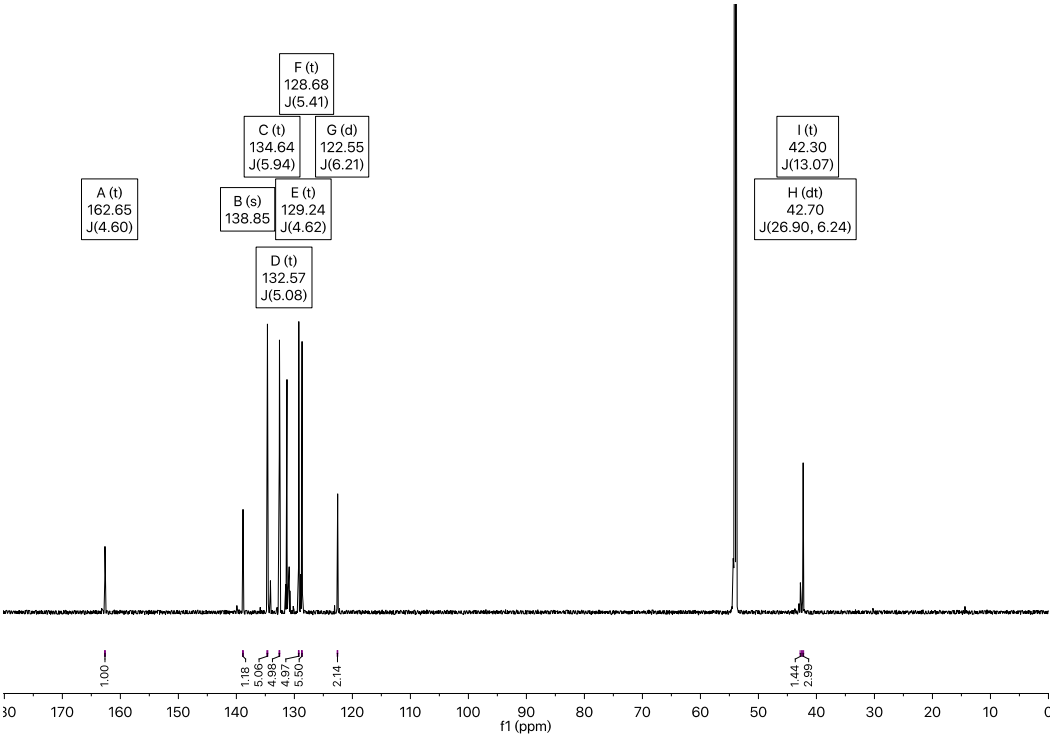

Figure S44. $_{13}$C{$_{1}$H} NMR spectrum of *cis*-($_{Ph}$PNP)Rh(CH_2Cl)(Cl)$_2$ (**4e-*cis***) in dichloromethane-d_2.

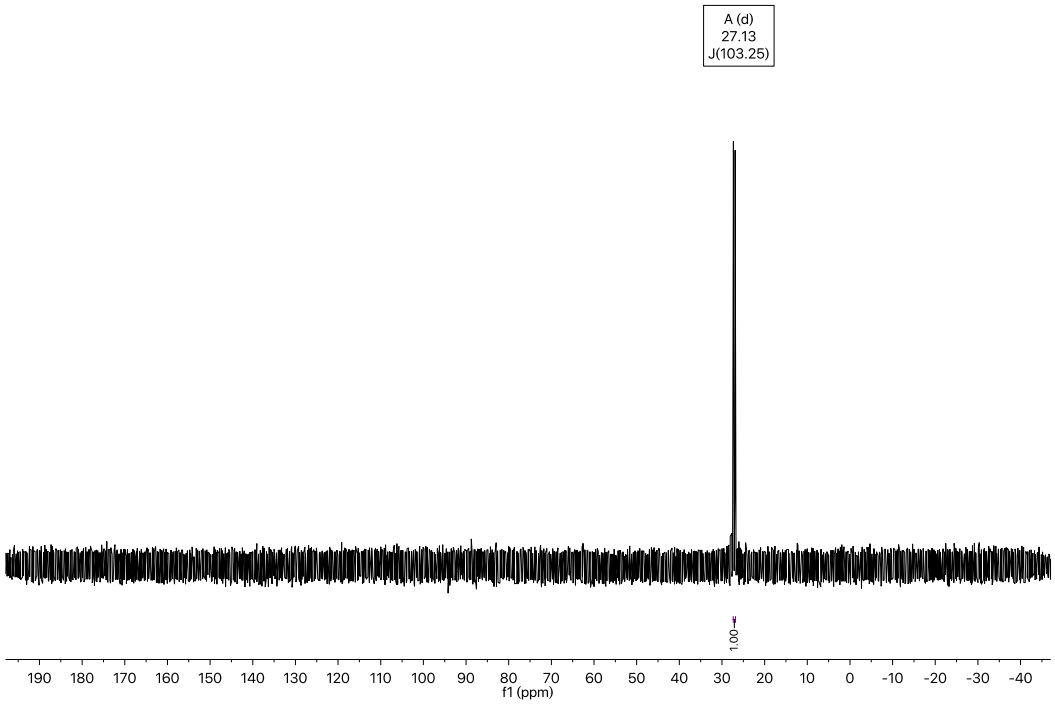

Figure S45. $^{31}P\{^{1}H\}$ NMR spectrum of *cis*-(^{Ph}PNP)Rh(CH_2Cl)(Cl)$_2$ (**4e-*cis***) in dichloromethane-d_2.

2. NMR Spectra and Plots of Kinetics Studies and Equilibrium Studies

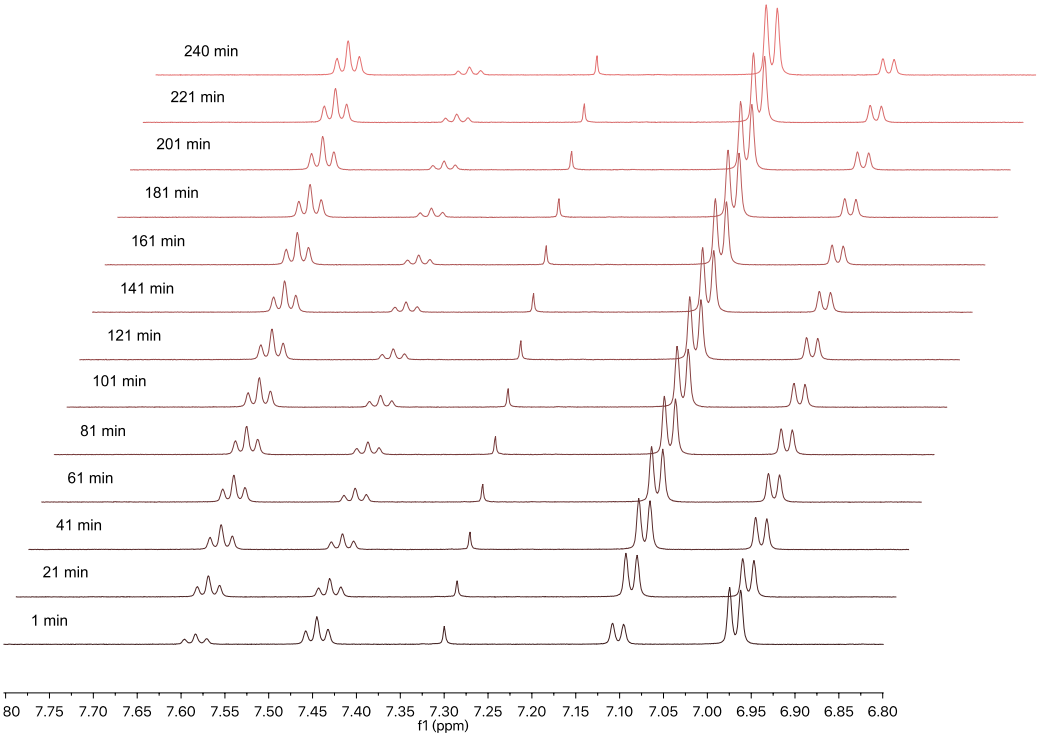

Figure S46. Pyridyl region of ^{1}H NMR spectra (THF-d_8, 600 MHz) of oxidative addition of MeI to (^{tBu}PNP)RhCl (**1a**) and the following reductive elimination at 300 K.

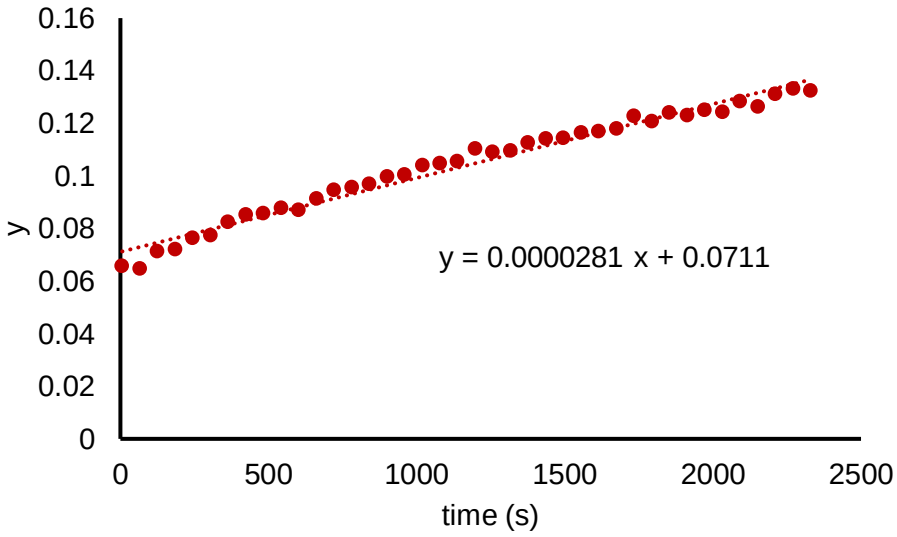

Figure S47. Second-order fit for the oxidative addition of MeI to **1a** at 327 K, where

$$y = \frac{1}{[\mathbf{1a}]_0 + [\mathrm{MeI}]_0} \ln \frac{[\mathbf{1a}]}{[\mathrm{MeI}]},$$

and the slope (m = 0.0000281) is the rate constant in $mM^{-1} \cdot s^{-1}$.

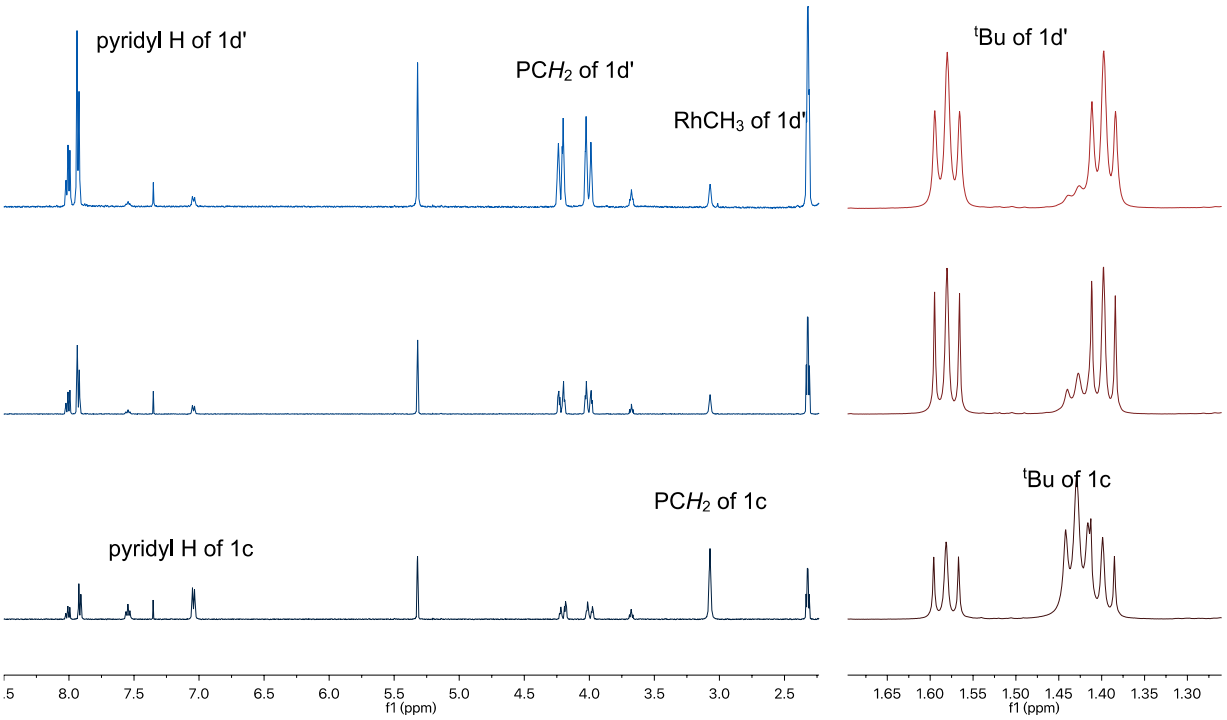

Figure S48. Pyridyl region (left) and *tert*-butyl region (right) from $_1$H NMR spectra (dichloromethane-d_2, 600 MHz) of the equilibrium between ($_{tBu}$PNP)RhI (**1c**), MeI and [($_{tBu}$PNP)Rh(Me)(I)](I) (**1d'**). From bottom to top, the concentration of MeI is 7.1 mM (0.48 equiv. to the sum of Rh complexes **1c** and **1d'**), 40 mM (2.7 equiv.) and 101 mM (6.8 equiv.) respectively.

3. Computational Methods Details

Below we compare the DFT calculated reaction free energies and activation barriers with those measured experimentally in this work and work by Goldberg et al.[1] on a similar addition of CH_3I to $(dppe)Pt(CH_3)_2$.

In reaction **A**, CH_3I is added to (^{tBu}PNP)RhI in dichloromethane.

In reaction **B**, CH_3I is added to (^{tBu}PNP)RhCl, then CH_3Cl is eliminated, in THF.

In reaction **C**, CH_3I is eliminated from $(dppe)Pt(CH_3)_3(I)$ in acetone.

To illustrate the performance of the chosen basis sets, solvation model, and two density functionals, we provide computed free energies (using M06-L and B3PW91-d3). These two functionals use distinctly different approaches to describing the weakly attractive London dispersion forces (van der Waals attraction) important when two molecules are brought together. B3PW91-d3 relies on the Grimme empirical corrections, while M06-L incorporates medium-range correlation through parameterized inclusion of the kinetic energy density.

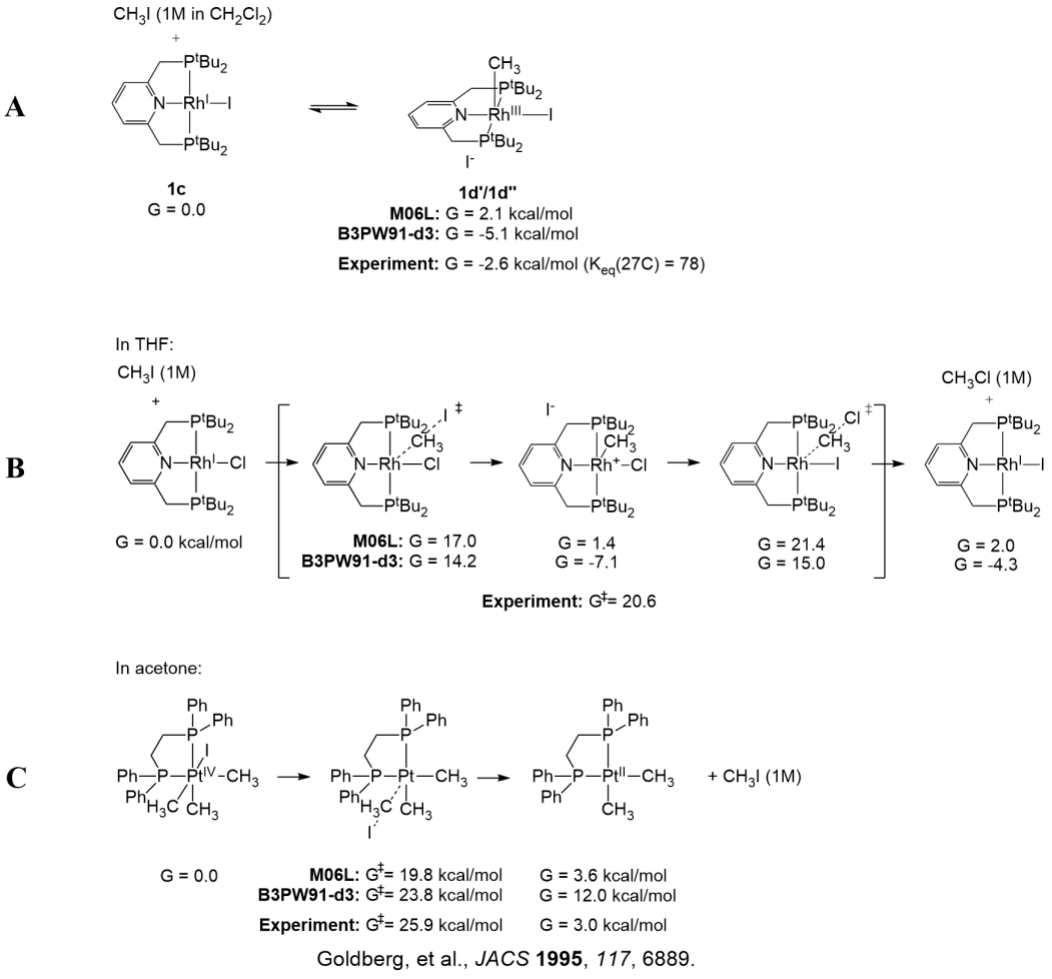

Scheme S1. Free energies and activation barriers: a comparison between this work and the work by Goldberg et al. **A.** oxidative addition of CH_3I on (^{tBu}PNP)RhI in CH_2Cl_2. **B.** Oxidative addition of CH_3I on

($_{tBu}$PNP)RhCl and the following reductive elimination in THF. **C.** Reductive elimination of CH_3I from (dppe)Pt(CH_3)$_3$(I) in acetone.

M06-L consistently favors the separated, reduced state ("L_nM + CH_3I") over the combined state ("$L_nM(CH_3)(I)$") relative to the B3PW91-d3 functional by about 8 kcal/mol. In reaction **A**, the experimental ΔG of -2.6 kcal/mol lies between the two predicted values, closer to B3PW91-d3 (ΔG = -5.1) than M06L (ΔG = 2.1). There is some uncertainty regarding the location of the unbound iodide in the Rh(III) product. Both functionals prefer the iodide on the opposite side of the PNP-plane (over the pyridine moiety) from the methyl group, rather than the same side as the methyl group. In reaction **C**, M06L correctly predicts ΔG (error of 0.6 kcal/mol) while B3PW91-d3 errs significantly (by 9 kcal/mol).

Comparing activation energies for reaction **B** is not straightforward, since B3PW91-d3 predicts the Rh(III) intermediate to dominate a pre-equilibrium with ($_{tBu}$PNP)RhCl even at low concentrations. Either functional can be argued to provide an accurate barrier of 21.4 kcal/mol (M06L) or 22.1 kcal/mol (15.0 – (-7.1), B3PW91-d3). In reaction **C**, B3PW91-d3 provides an accurate barrier only for the elimination reaction, not the reverse, while M06L underestimates the reaction barrier in both directions.

Steinmetz and Grimme benchmarked the performance of many DFT functionals for reaction energies and barriers for oxidative addition of small molecules to Pd_0 and Pd_{II} centers.[2] They showed that the M05 and M06 suite of functionals generally favor reduced states, and that among these only the M06-L functional performs well for reaction energies and barrier heights.

4. Crystal Structure Data

Table S1. Crystal structure data table for **1c**, **2a**, **2b** and **2e**.

	1c	**2a**	**2b**	**2e**
CCDC	1948889	1948890	1948891	1948892
Chemical formula	$C_{23}H_{43}INP_2Rh$	$C_{19}H_{35}ClNP_2Rh$	$C_{20}H_{38}ClINP_2Rh$	$C_{26}H_{43}Cl_3NP_2Rh$
FW (g/mol)	625.33	477.78	619.71	640.81
T (K)	150(2)	100(2)	100(2)	100(2)
λ (Å)	0.71073	0.71073	0.71073	0.71073
Crystal size (mm)	0.054 x 0.080 x 0.539	0.098 x 0.103 x 0.682	0.130 x 0.277 x 0.335	0.151 x 0.167 x 0.206
Crystal habit	red rod	red rod	yellow plate	orange block
Crystal system	hexagonal	trigonal	monoclinic	monoclinic
Space group	P $6_5$22	R -3c	P 2_1/n	P 2_1/n
a (Å)	16.6377(18)	25.458(2)	12.6728(19)	12.6845(12)
b (Å)	16.6377(18)	25.458(2)	10.0381(15)	10.7686(10)
c (Å)	19.370(2)	20.014(2)	19.476(3)	22.2617(19)
α (°)	90	90	90	90
β (°)	90	90	102.263(4)	105.759(3)
γ (°)	120	120	90	90
V (Å$_3$)	4643.5(11)	11233.(2)	2421.0(6)	2926.5(5)
Z	6	18	4	4
ρ_{calc} (g/cm$_3$)	1.342	1.271	1.700	1.454
μ (mm^{-1})	1.661	0.921	2.229	0.983
θ range (°)	1.41 to 26.40	2.23 to 27.57°	1.76 to 28.33°	1.68 to 28.31°
Index ranges	-20 ≤ h ≤ 20 -20 ≤ k ≤ 20 -24 ≤ l ≤ 21	-30≤ h ≤ 26 -30 ≤ k ≤ 33 -26 ≤ l ≤ 26	-16 ≤ h ≤ 16 -13 ≤ k ≤ 13 -25 ≤ l ≤ 25	-16 ≤ h ≤ 16 -14 ≤ k ≤ 14 -29 ≤ l ≤ 29
Reflns coll.	34792	35978	27711	35089
Ind. reflns	3179 [R_{int} = 0.0651]	2882 [R_{int} = 0.0624]	6035 [R_{int} = 0.0464]	7261 [R_{int} = 0.0479]
Data / restraints / parameters	3179 / 0 / 135	2882 / 0 / 115	6035 / 2 / 251	7261 / 0 / 304
Goodness-of-fit on F_2	1.073	1.119	1.087	1.074
R_1 [I>2σ(I)]	0.0323	0.0268	0.0436	0.0411
wR_2 [all data]	0.0802	0.0499	0.0665	0.0951

Table S2. Crystal structure data table for **3a**, **3c**, **3d''**, **4b-1** and **4e-*cis***.

	3a	**3c**	**3''**	**4b-1**	**4e-*cis***
CCDC	1948893	1948894	1948895	1948896	1948897
Chemical formula	$C_{51}H_{67}ClNO_2P_2Rh$	$C_{52}H_{71}INOP_2Rh$	$C_{43.33}H_{51}I_{2.33}NP_2Rh$	$C_{32}H_{30}ClINP_2Rh$	$C_{32}H_{29}Cl_3NP_2Rh$
FW (g/mol)	926.35	1017.84	1046.68	755.77	698.76
T (K)	100(2)	100(2)	100(2)	100(2)	100(2)
λ (Å)	0.71073	0.71073	0.71073	0.71073	1.54178
Crystal size (mm)	0.164 x 0.195 x 0.546	0.054 x 0.124 x 0.386	0.055 x 0.107 x 0.417	0.056 x 0.085 x 0.089	0.057 x 0.096 x 0.217
Crystal habit	red rod	orange rod	orange rod	yellow plate	yellow plate
Crystal system	orthorhombic	orthorhombic	triclinic	triclinic	monoclinic
Space group	P $na2_1$	P $na2_1$	P -1	P -1	C 2/c
a (Å)	13.9434(9)	14.1036(10)	12.1678(8)	10.8043(15)	19.9996(10)
b (Å)	15.8571(11)	21.5216(14)	18.4729(12)	11.4622(16)	10.8688(7)
c (Å)	20.6401(12)	16.4282(10)	19.8742(13)	13.4978(19)	13.6976(9)
α (°)	90	90	105.184(2)	95.317(4)	90
β (°)	90	90	106.763(2)	90.973(5)	99.157(5)
γ (°)	90	90	92.623(2)	117.568(4)	90
V ($Å_3$)	4563.6(5)	4986.5(6)	4092.3(5)	1472.0(4)	2939.5(3)
Z	4	4	4	2	4
ρ_{calc} (g/cm_3)	1.348	1.356	1.699	1.705	1.579
μ (mm_{-1})	0.544	1.062	2.286	1.851	8.416
θ range (°)	1.62 to 28.32	1.56 to 26.41°	1.35 to 27.59°	1.52 to 25.78°	4.48 to 66.57°
Index ranges	-15 ≤ h ≤ 18 -21 ≤ k ≤ 18 -27 ≤ l ≤ 27	-17 ≤ h ≤ 16 -20 ≤ k ≤ 26 -20 ≤ l ≤ 20	-15 ≤ h ≤ 15 -22 ≤ k ≤ 24 -25 ≤ l ≤ 25	-9 ≤ h ≤ 13 -13 ≤ k ≤ 13 -16 ≤ l ≤ 16	-19 ≤ h ≤ 23 -12 ≤ k ≤ 11 -16 ≤ l ≤ 16
Reflns coll.	50779	43201	74612	23325	9565
Ind. reflns	11347 [R_{int} = 0.0375]	10008 [R_{int} = 0.0775]	18899 [R_{int} = 0.0818]	5620 [R_{int} = 0.1092]	2605 [R_{int} = 0.1387]
Data / restraints / parameters	11347 / 1 / 535	10008 / 17 / 511	18899 / 0 / 925	5620 / 0 / 346	2605 / 0 / 180
Goodness-of-fit on F_2	1.036	1.048	1.027	1.038	1.047
R_1 [I>2σ(I)]	0.0298	0.0557	0.0488	0.0617	0.0723
wR_2 [all data]	0.0711	0.1513	0.1456	0.1431	0.2062

References:

1. Goldberg, K. I.; Yan, J.; Breitung, E. M. Energetics and Mechanisms of Carbon-Carbon and Carbon-Iodide Reductive Elimination from a Pt(IV) Center. *J. Am. Chem. Soc.* **1995,** *117*, 6889-6896.

2. Steinmetz, M.; Grimme, S. Benchmark Study of the Performance of Density Functional Theory for Bond Activations with (Ni,Pd)-Based Transition-Metal Catalysts. *ChemistryOpen* **2013,** *2*, 115-124.